Lehigh University
Lehigh Preserve

Theses and Dissertations

2019

Hydrogen Centers in Semiconductor Oxides In2O3 and Ga2O3 Studied by FTIR Spectroscopy

Ying Qin
Lehigh University, qin.ying08nku@gmail.com

Follow this and additional works at: https://preserve.lehigh.edu/etd

 Part of the Physics Commons

Recommended Citation

Qin, Ying, "Hydrogen Centers in Semiconductor Oxides In2O3 and Ga2O3 Studied by FTIR Spectroscopy" (2019). *Theses and Dissertations*. 5614.
https://preserve.lehigh.edu/etd/5614

This Dissertation is brought to you for free and open access by Lehigh Preserve. It has been accepted for inclusion in Theses and Dissertations by an authorized administrator of Lehigh Preserve. For more information, please contact preserve@lehigh.edu.

Hydrogen Centers in Semiconductor Oxides In_2O_3 and Ga_2O_3 Studied by FTIR Spectroscopy

by

Ying Qin

A Dissertation
Presented to the Graduate Committee
of Lehigh University
in Candidacy for the Degree of
Doctor of Philosophy
in
Physics

Lehigh University
January 2019

Copyright
Ying Qin

Approved and recommended for acceptance as a dissertation in partial fulfillment of the requirements for the degree of Doctor of Philosophy.

Ying Qin
Hydrogen Centers in Semiconductor Oxides In_2O_3 and Ga_2O_3 Studied by FTIR Spectroscopy

---

Date

Dr. Michael J. Stavola, Dissertation Director, Chair
(Must Sign with Blue Ink)

Accepted Date

Committee Members

Dr. W. Beall Fowler

Dr. Gary Deleo

Dr. Ivan Biaggio

Dr. Richard Vinci

Five years seems like a long time. It is 17.24% of my lifetime so far to be precise. However it also passed by faster than I had imagined. Looking back, it is the following people that made my time at Lehigh not only enjoyable but also meaningful.

The first person I owe my gratitude to is, no doubt, Dr. Michael Stavola who is my advisor and my mentor. His guidance and kindness inspire me to be a better researcher and more importantly, a better person.

I would also like to thank my committee members, Dr. Fowler, Dr. Deleo, Dr. Biaggio, and Dr. Vinci for their encouragement, interest and thoughtful comments, especially, Dr. Deleo for his kindness when I was in need of help.

To my group members, Dr. Philip Weiser and Dr. Weikai Yin, it is their daily support and friendship that made my time in the lab less lonely. And to my dearest friend, Dr.Thienbao Nguyen Carpency, I cannot thank you enough for all the ups and downs we had together. Also to my best friends from undergraduate, Dr. Jingyin Jiang, and Jingyi Wang, thank you for always being there for me.

And thank you to everyone I have encountered in the Physics Department, my fellow graduate students, faculty and staff members, who truly made our department a family. In particular, I really appreciate all the help from John Gregoris over the years.

And last but certainly not the least, this work is dedicated to my parents, Shuping Ma and Guilin Qin, who let their only daughter leave home to pursue the life she wanted.

Contents

List of Tables

List of Figures

Abstract

Hydrogen is found to be an n-type dopant in In_2O_3 that gives rise to unintentional conductivity. An infrared (IR) absorption line observed at 3306 cm^{-1} is assigned to the H_i^+ center. We have performed two types of experiments to determine the diffusivity of H_i^+ in In_2O_3 from its IR absorption spectra. (i) At temperatures near 700 K, the O-H line at 3306 cm^{-1} is used to determine the diffusivity of H_i^+ from its in-diffusion and out-diffusion behaviors. (ii) At temperatures near 160 K, stress has been used to produce a preferential alignment of the H_i^+ center that has been detected in IR absorption experiments made with polarized light [1]. With the help of theory, the kinetics with which a stress-induced alignment can be produced yield the time constant for a single jump of the H_i^+ center and also the diffusivity of H_i^+ near 160 K. The combination of the diffusivity of H_i^+ found near 700 K by mass-transport measurements and that found near 160 K from the time constant for a single H_i^+ jump determines the diffusivity for H_i^+ over eleven decades!

Hydrogen has a strong influence on the electrical properties of transparent conducting oxides where it can give rise to shallow donors and can passivate deep compensating defects. Vibrational spectroscopy has shown that the introduction of H into Ga_2O_3 produces a dominant hydrogen center with a strongly polarized vibrational line at 3437.0 cm^{-1}. Theory assigns the 3437.0 cm^{-1} line to a defect with two equivalent H atoms trapped at a relaxed Ga vacancy. We also produced a reservoir of additional hydrogen defects in Ga_2O_3 by annealing treatments in an H_2 ambient followed by rapid cooling. These additional defects are not as thermally stable as the V_{Ga}-2H center and have different polarization properties. Some of these defects appear to be shallow donors and others appear to be V_{Ga}-H complexes

with structures different than the 3437.0 cm^{-1} center. These additional defects can be converted into the V_{Ga}-2H defect by annealing in an inert ambient.

Chapter 1

Introduction

1.1 Transparent Conducting Oxides (TCOs)

Transparent conducting oxides (TCOs) are a class of semiconducting oxides that have unusual but highly useful properties, combining transparency in the visible region of the spectrum with high electrical conductivity. These properties are achieved by their wide band-gap and their intrinsic defects or extrinsic dopants. Most of the useful oxide-based semiconductors are n-type materials with a wide band-gap ($> 3\ eV$), and a balance between optical transparency and electrical conductivity. They are widely used as transparent electrode materials and as wide band-gap semiconductors.

Indium tin oxide (ITO, 90% In_2O_3, 10% SnO_2 by weight) is the most widely used transparent conducting oxide because of its remarkable combination of optical and electrical properties along with high environmental stability and process controllability [2]. Fig. 1.1 shows indium tin oxide coated glass; it is ITO on a passivation layer(SiO_2) on glass. ITO coated glass is a type of TCO coated substrate. The uniform thin layer of ITO over a glass substrate makes it highly transparent and with low surface resistance. Therefore ITO is often used for transparent conductive coatings for optoelectronic devices and flat-panel displays.

Figure 1.1: Indium Tin Oxide coated glass slides TIX series by TECHINSTRO Co. Specified ITO Sheet resistivity $\leq$ 10 $ohms/sq$; Transmittance at 550 nm $\geq$ 83 %. `http://techinstro.blogspot.com/2014/07/indium-tin-oxide-coated-glass-slides.html`.

1.2 Vibrational spectroscopy of hydrogen centers

1.2.1 Local vibrational modes (LVMs)

For the purpose of identifying defects and impurities in a host crystal, the vibrational modes of defects in solids have been widely studied [3]. The basic ideas about the different vibrational modes can be illustrated with a simple diatomic chain model: defect is introduced by replacing the atom m by a new atom of mass m' bound to its neighbors by the same force constant as before. The different vibrational modes of this linear chain are shown in Fig.1.2 [4]. Due to the light element impurity, a new vibrational mode emerges from the phonon band at high frequency. The host atoms are too heavy to follow the high vibrational frequency of the light atom so the mode does not propagate. Only the impurity and its first neighbors vibrate appreciably; this is known as a local vibrational mode (LVM).

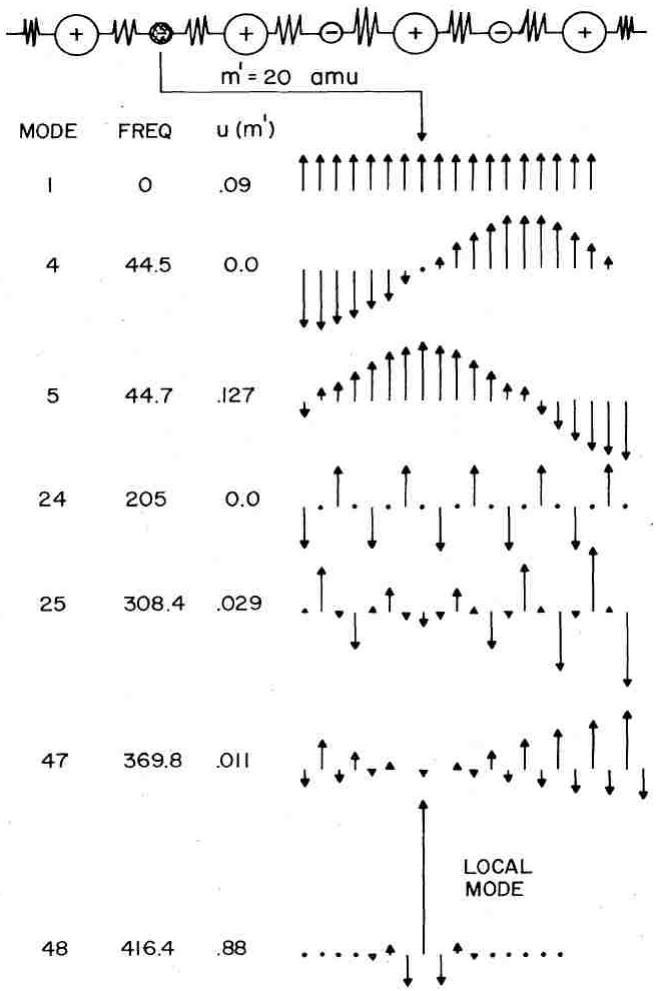

Figure 1.2: Diatomic linear chain model that contains an impurity with mass m' that substitutes for a lattice atom with mass m. The normal vibrational modes of the chain are shown.

1.2.2 Isotope shifts

The vibrational frequency, ω, of a diatomic "defect molecule" which consists of the light impurity with mass m', and its nearest neighbor host atom with mass M_{nn}, is given by Eq. 1.1:

$$\omega^2 = k(\frac{1}{m'} + \frac{1}{XM_{nn}}). \tag{1.1}$$

Here, k is a force constant and X is a parameter that accounts for the number of nearest neighbors and for the binding of the nearest-neighbor atoms to the rest of the crystal. For many LVMs, X has been typically found to be near 2 [5]. Combining Eq. 1.1 with isotope substitution allows the masses of the light impurity and of the heavy host atom to be identified through their vibrational frequencies.

In the case of a defect that contains more than one light-mass element, isotopic substitution reveals the coupling of identical modes (or modes that are close in frequency). For example, a defect that contains two identical H (or D) atoms will have two coupled O-H (or O-D) modes. If both H and D are introduced into the host material, there will also be defects formed with both H and D. The O-H and O-D modes of the defect become dynamically decoupled and give rise to new vibrational lines for the decoupled oscillators due to the large difference in the masses of H and D.

1.2.3 Fourier Transform Infrared Spectroscopy (FTIR)

Infrared (IR) spectroscopy is an experimental technique that can probe the vibrational transitions in a material. It yields an infrared spectrum of absorption or photo-conductivity by utilizing the interaction of light with frequencies in the IR domain ($\backsim 10 - 10,000\, cm^{-1}$) and the material of interest.

In IR absorption experiments, the quantity measured, T, is the ratio of incident and transmitted beam intensities [6]

$$T = \frac{I}{I_0} = \frac{(1-R)^2 + 4Rsin^2\psi}{e^{\alpha x} - R^2 e^{-\alpha x}} \tag{1.2}$$

$$\alpha = \frac{4\pi k}{\lambda} \tag{1.3}$$

Here α is the absorption coefficient, k is the extinction coefficient, and x is the sample thickness (assumed homogeneous). R is the reflectivity from a single surface of the sample and is related to the refractive index n and the extinction coefficient k by the relationship [6] [7]

$$R = \frac{(n-1)^2 + k^2}{(n+1)^2 + k^2}. \tag{1.4}$$

The value of $\psi = tan^{-1}\frac{2k}{n^2+k^2-1}$ is small, since for $\alpha < 10^3 cm^{-1}$ the value of k is much smaller than 1. Therefore the term $4Rsin^2\psi$ can usually be neglected. The transmission T is then given by [8]:

$$T = \frac{I}{I_0} = \frac{(1-R)^2 e^{-\alpha x}}{1 - R^2 e^{-2\alpha x}} \tag{1.5}$$

High values of $\frac{I}{I_0}$, corresponding to small αx, approach $\frac{1-R}{1+R}$, whereas low values of $\frac{I}{I_0}$ vary almost exponentially with αx and extrapolate to $(1-R)^2$ at $x = 0$ [6]. T is often approximated by to the following expression:

$$T \cong (1-R)^2 e^{-\alpha x} \tag{1.6}$$

Fourier Transform Infrared (FTIR) spectrometers are now widely used to measure IR absorption spectra and have much greater sensitivity and resolution than dispersive spectrometers [9]. The most common setup uses a Michelson interferometer, shown in Fig. 1.3, in which collimated light is separated into two beams by a beam splitter. Each beam is reflected from a mirror, recombines at the beam splitter, and is passed to the detector. An optical path difference between the two beams is created by fixing one mirror and translating the other, which results in an interference pattern. The output of light intensity vs. distance the mirror travels from the zero path difference (ZPD) is the interferogram, which is converted to a frequency domain spectrum via a Fourier Transform. The frequency, $\overline{\nu}$, is often given in wavenumber (cm^{-1}) units, where $\overline{\nu} \equiv \frac{1}{\lambda}$ is the reciprocal of the wavelength. The configuration of our Bomem DA 3.16 spectrometer is shown in Fig. 1.4 [10]. Examples of an interferogram and its frequency domain spectrum are shown in Fig. 1.5.

It is worth noting that in Eq. 1.5, an interference oscillation that can occur for a sample with plane-parallel front and back surfaces has been neglected [11]. This can typically be reduced by wedging one of the sample's surfaces at an angle of a few degrees or by eliminating sharp peaks in an interferogram before performing the Fourier transform to obtain a spectrum. The Bomem spectrometer calculates the absorbance spectrum A defined as:

$$A = -log_{10}(T) \tag{1.7}$$

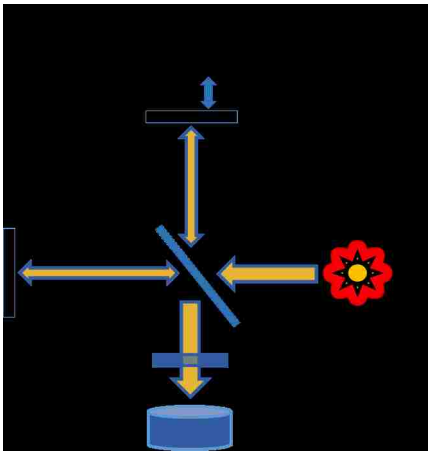

Figure 1.3: Optical configuration of a Michelson interferometer

For the characterization of a specific defect, the quantity α_d, the defect's absorption coefficient, is of importance. To be able to extract α_d from α in Eq. 1.6, a reference spectrum for a sample of the same host material without the specific defect is measured. α_d then is given by

$$\alpha_d \cong x^{-1} ln \left(\frac{T_R}{T_S} \right) \tag{1.8}$$

where T_R is the transmission spectrum for the reference sample and T_S is the transmission spectrum for the sample containing the defect of interest.

So far, samples have been assumed to be homogeneous. In the case where the layer thickness is not well defined, instead of the absorption coefficient α_d, an absorbance spectrum A_d can be measured as [11]

$$A_d = A_S - A_R = log_{10} \left(\frac{T_R}{T_S} \right) \tag{1.9}$$

It is also useful to be able to determine the concentration of a defect from its LVM spectrum. The area of a vibrational absorption band (i.e., the integrated absorption coefficient) is proportional to the concentration of the associated defect

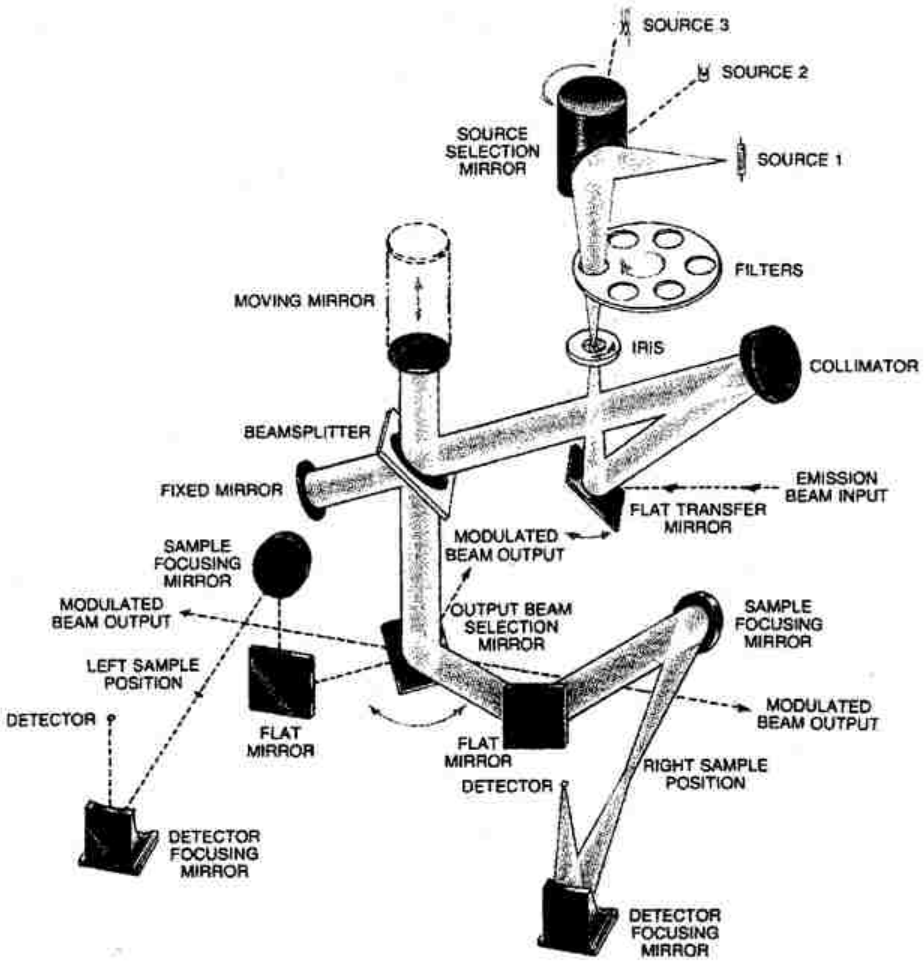

Figure 1.4: Optical configuration of the Bomem DA 3.16 spectrometer. Most of our experiments utilize a globar source, a KBr beam splitter, and a liquid nitrogen cooled InSb detector to investigate the OH (OD) vibrational modes that occur in the $\backsim 1,800 - 6,000\, cm^{-1}$ region.

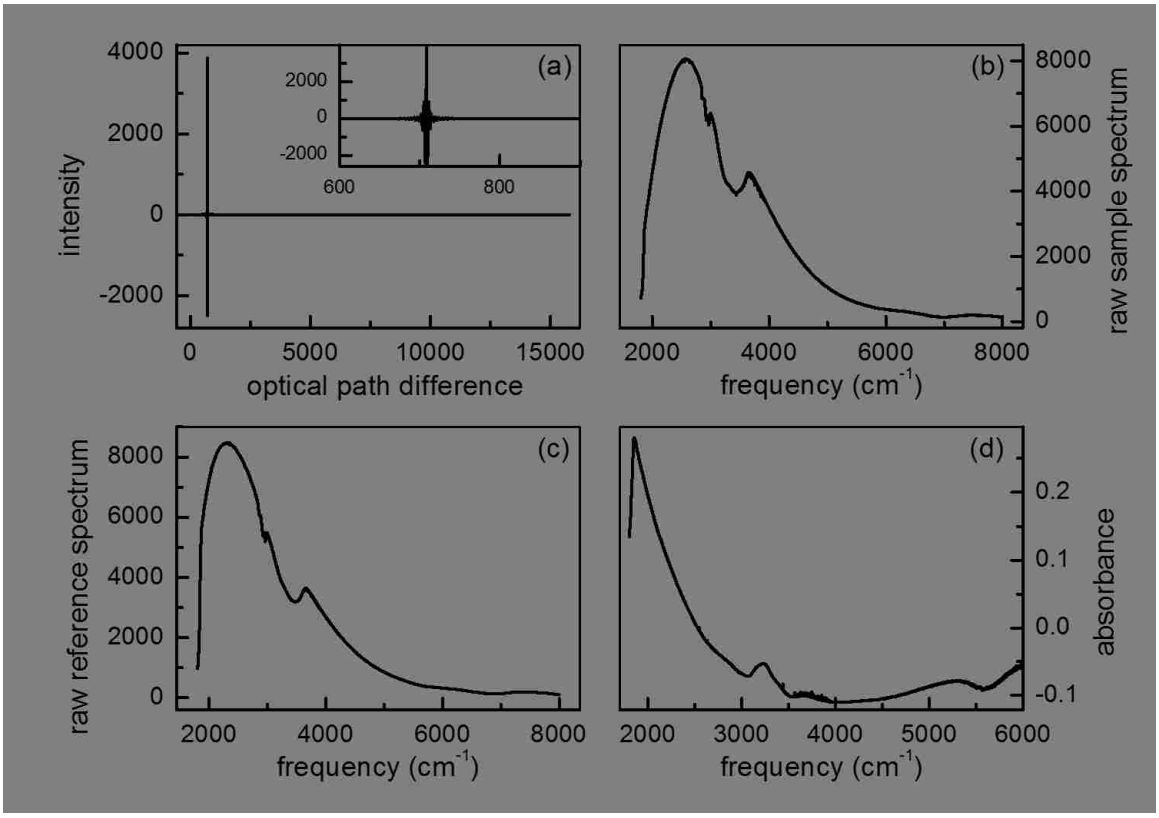

Figure 1.5: (a) Interferogram and (b) the corresponding Fourier transformed spectrum. The bottom two panels are (c) reference and (d) absorbance spectra.

and is given by [12]

$$\int \alpha\left(\bar{\nu}\right) d\bar{\nu} = \frac{\left(\pi q^2 N\right)}{\left(\mu n c^2\right)} \tag{1.10}$$

Here, concentration N is in units cm^{-3}, absorption coefficient α in cm^{-1}, and the frequency $\bar{\nu}$ in cm^{-1}. μ is the reduced mass of the vibrating impurity, n is the refractive index of the host crystal, and c is the speed of light. And q, typically expressed as a multiple of the electron charge e, is a parameter called the effective oscillating charge which is the change in the dipole moment per unit displacement of the normal coordinate of the LVM. An independent calibration is needed to accurately calculate the concentration for a defect from LVM spectroscopy. Such a

calibration is necessary to relate N to the absorption strength due to the fact that q is unknown [3]. Secondary ion mass spectrometry (SIMS), Hall effect [13], and activation analysis have all been used to determine q which has been found to be roughly in the range $0.3\,e - 3\,e$ [5] [14].

1.2.4 Free carrier absorption (FCA)

In semiconductors, the effect of free carriers on the optical properties [15] [16] becomes important at wavelengths longer than the intrinsic absorption edge. It is typically observed in the near-infrared spectral region where the semiconductor would normally be transparent [7]. The absorption owing to the presence of free carriers (FCA) happens at frequencies above the plasma frequency ω_p below which the reflectivity of a gas of free electrons is $100\,\%$.

FCA is often described based on the phenomenological Drude model which is used to describe the behavior of free valence electrons in metals. To apply this model to doped semiconductors, two modifications are made: electrons and holes are moving in the conduction or valence band with an effective mass m^* instead of the free electron mass m_0; bound electrons also contribute to the dielectric constant due to their optical response. The absorption coefficient for free carriers can be deduced [7] using Eq. 1.3 and expressions for n and k calculated from the complex dielectric constant in the modified Drude model.

$$\alpha_{fc} = \frac{Ne^2}{m^*\epsilon_0 nc\tau}\frac{1}{\omega^2} \tag{1.11}$$

where ϵ_0 is the electric permittivity of free space, n the refractive index, τ the damping time or the momentum scattering time as a result of the damping of the free carrier oscillations. Eq. 1.11 shows that the FCA is proportional to the carrier density N and should vary with frequency as ω^2.

Fig. 1.6 [7] illustrates the physical processes that are occurring during free carrier absorption. It shows an electron being excited by a photon($\hbar\omega$) from below the Fermi level (E_F) to an unoccupied state above E_F. The electron then has to be scattered to conserve momentum since the photon has a very small momentum compared to the electron.

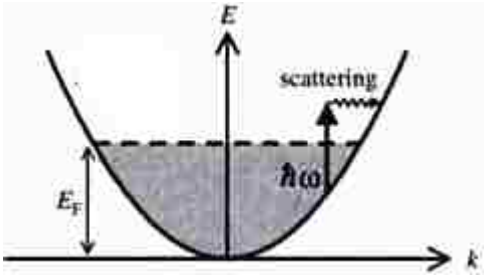

Figure 1.6: A free carrier transition in a doped semiconductor.

FCA is an important characteristic of semiconductors because of its proportionality to the carrier concentration. It provides information about the electrical activity of a defect by giving rise to broad low-frequency absorption that we detect by IR spectroscopy for use as a contact-free strategy to probe conductivity.

1.3 Effect of hydrogen in TCOs

Hydrogen is ubiquitous in the environment, and has an important effect on the electrical properties of semiconductors and participates in a rich variety of phenomena.

1.3.1 Doping rather than passivation

The hydrogen-passivated donor and acceptor impurities in conventional semiconductors (i.e. Si, GaAs) are well-known [17]. Hydrogen introduces electrical levels in the band-gap of semiconductors, has different configurations in its different charge states, forms complexes with shallow- and deep-level defects, and can also give rise to other H-containing defects such as H_2 molecules.

In contrast, hydrogen has been deemed responsible, in several cases, for the n-type conductivity in TCOs. It acts as a shallow donor and can dramatically affect the electrical properties of oxides. Two types of hydrogen shallow donors have been predicted [18–23]: Interstitial H_i and substitutional H_o. H_i forms a strong O-H

bond with stretching frequencies near 3500 cm^{-1}. H_o is hydrogen trapped at an oxygen vacancy and gives rise to a multicenter bond with a much lower vibrational frequency that has made H_o challenging to study by vibrational spectroscopy [20].

Hydrogen can also form complexes with acceptor dopants and cation vacancies in TCOs [24], and can exist as H_2 molecules which are electrically neutral and do not absorb IR light [25, 26].

1.3.2 ZnO as an example, H_i, H_o, H_2, free carrier absorption

ZnO has the hexagonal wurtzite crystal structure and is a wide band-gap (3.4 eV) semiconductor that is widely used in electronic and optoelectronic devices [27]. Historically, the unintentional n-type conductivity in ZnO was attributed to native defects (zinc interstitials Zn_i and oxygen vacancies V_o). It was not until recent studies (the 2000s) that hydrogen became the center of attention for being an excellent candidate for shallow donor in ZnO [18].

Hydrogen can give rise to both H_i and H_o shallow donors whose properties have been investigated extensively by theory and experiment. An O-H vibrational line at 3611 cm^{-1}, with a transition moment oriented along the c axis of ZnO, and the corresponding O-D line at 2688 cm^{-1} were found [28]. The 3611 cm^{-1} line is eliminated by an anneal near 150^0C and is assigned to the H_i shallow donor [29–31]. It is also found that, at 150^0C, interstitial H_2 molecules ("hidden hydrogen") are formed while the H_i lines are annealed away. Furthermore, annealing studies showed that H_i can be interconverted between the species that is hidden from IR spectroscopy and the H_i defect which gives rise to O-H lines [25, 26].

An additional, more thermally stable ($\approx 500^0C$) hydrogen shallow donor is found in ZnO [29–31] which has been predicted by theory to be H_o that forms a novel multicenter bond where H is weakly bounded to four Zn neighbors [20]. The vibrational mode predicted for H_o lies in a region where ZnO is strongly absorbing and is difficult to study [20]. Photothermal-ionization spectroscopy (PTIS) was used to detect the vibrational modes of H_o at 742 cm^{-1} and 792 cm^{-1} [32] in photoconductivity spectra.

Furthermore, two additional infrared absorption lines at 3349.6 cm^{-1} and 3312.2 cm^{-1} have been detected and are associated with a hydrogenated Zn vacancy ($V_{Zn}H_2$ by first-principles calculations [28]. More recently, another hydrogen-related defect in ZnO which leads to two broad IR absorption bands at 3303 cm^{-1} and 3321 cm^{-1} has been assigned to the LVMs of a defect consisting of three equivalent hydrogen atoms-$V_{Zn}H_3$ [33].

The preceding background information provides a brief survey of how hydrogen defects in transparent conducting oxides can be studied by using Fourier-transform infrared spectroscopy.

Chapter 2

Diffusion of hydrogen in In_2O_3

2.1 In_2O_3

In_2O_3 is a transparent conducting oxide that finds broad application in flat-panel displays and as transparent electrodes for electronic devices such as light emitting diodes and solar cells [34, 35]. While $In_xSn_{1-x}O$ (ITO) is a commonly used conducting film, hydrogen impurities have also been found to be an important source of n-type conductivity in In_2O_3. Theory predicts that both interstitial hydrogen (H_i) and hydrogen trapped at an oxygen vacancy can be shallow donors [22]. Implanted muons, whose properties mimic those of hydrogen, have also been found to form shallow donors in In_2O_3 [36]. Furthermore, In_2O_3: H can be used to fabricate conductive films with greater transparency than ITO in the infrared (IR) region of the spectrum and has attracted attention for solar-cell applications [37–39].

In_2O_3 has the cubic bixbyite structure with a conventional unit cell that contains 80 atoms [34]. Reference [22] provides details about the bixbyite structure.

Our recent research on the H_i^+ center in In_2O_3 has helped us to develop strategies for measuring its diffusivity with vibrational spectroscopy [1]. In this chapter, the diffusivity of H_i^+ in In_2O_3 single crystals is determined over a range greater than 11 decades from the hydrogen-diffusion profiles investigated in mass transport experiments and from the time constant for single hydrogen jumps investigated in

stress-alignment experiments. It is also important to point out that the study of the 3306 cm^{-1} line lets us make diffusion measurements specific to the isolated H_i^+ shallow donor without contributions from other hydrogen defects in In_2O_3.

2.2 H_i shallow donor assignment

Samples treated in an H_2 ambient show a vibrational line seen at 3306 cm^{-1} (Fig. 2.1). This line was found to be correlated with infrared (IR) absorption due to the free carriers that were also produced by the hydrogen treatment [40]. The 3306 cm^{-1} line has been assigned to the lowest energy O-H antibonding configuration, AB_{01}, for H_i^+ predicted by theory [Fig. 2.2(a)] [22, 40]. (There are three additional metastable antibonding hydrogen sites associated with each oxygen atom.) Subsequent IR absorption experiments performed in conjunction with applied uniaxial stresses revealed a C_{1h} symmetry for the 3306 cm^{-1} defect, supporting this assignment [1].

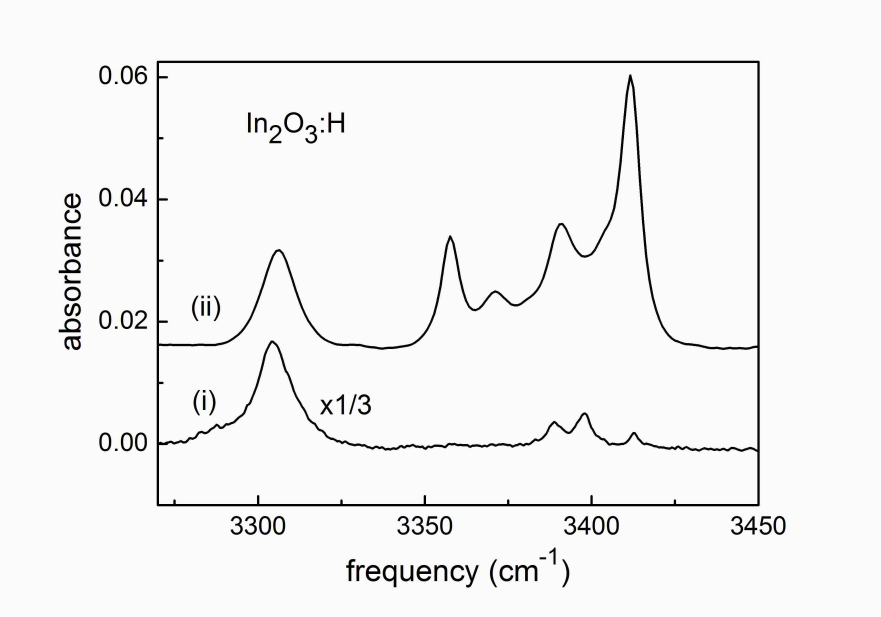

Figure 2.1: IR absorption spectra ($4.2\,K$, resolution $= 1\,cm^{-1}$) for In_2O_3 samples containing hydrogen. The lower spectrum (i) shows the $3306\,cm^{-1}$ line for a sample that was hydrogenated intentionally by an anneal in an H_2 ambient at $698\,K$ for $2\,h$. The upper spectrum (ii) shows the $3306\,cm^{-1}$ line assigned to $H_i{}^+$ for a sample containing hydrogen introduced unintentionally during growth.

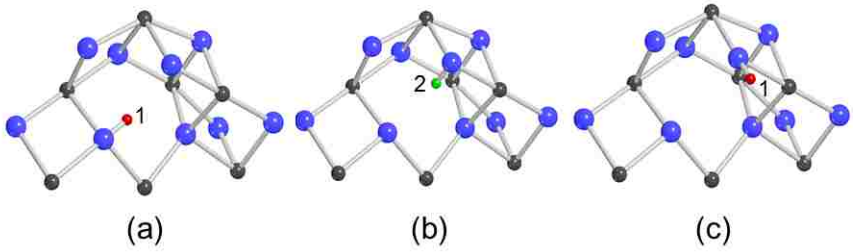

Figure 2.2: Defect models showing the pathway for a diffusion jump of H_i^+ in In_2O_3 predicted by theory. The atoms are color coded as follows: H, red and green; In, black; O, blue. (a) The lowest energy configuration for H_i^+, AB_{01}. (b) A metastable configuration, AB_{02}, that lies 0.51 eV higher in energy. (c) A near-lying AB_{01} site. The motion of H_i^+ from the configuration shown in (a) to the configuration shown in (c) by way of the metastable configuration shown in (b) is predicted to be a two-step, diffusion-jump process. This figure was constructed by MOLDRAW (P. Ugliengo, Torino 2006, available at `http://www.moldraw.unito.it`) and POV-Ray (`http://povray.org`).

2.3 Brief review of stress studies

The perturbation of the vibrational properties of H_i^+ in In_2O_3 created by applying uniaxial stress[41] reveals experimentally the symmetry of H_i^+, its transition moment direction, and, with the help of theory, the mechanism and activation energy for a hydrogen diffusion jump [1].

The In_2O_3 crystals that were grown at ORNL for these experiments were large enough to enable IR absorption measurements to be made in conjunction with applied uniaxial stresses. Defects with symmetries lower than the site symmetry of a host crystal have several crystallographically equivalent orientations [41, 42]. Low temperature IR absorption measurements made with polarized light as a function of the applied stress determine how the IR lines associated with orientationally degenerate defects are split. Stress experiments have determined that the H_i^+ center giving rise to the 3306 cm^{-1} line has C_{1h} symmetry [1, 43]. Furthermore, under an applied stress, the differently oriented defects have different ground state energies, so the application of stress provides a strategy for producing a preferential alignment of a defect that can be detected by the absorption of polarized light [41, 44]. For a defect that can be aligned, the kinetics for its reorientation in annealing experiments can be measured to investigate its motion [45]. Previous experiments at a temperature of 165 K performed by Philip Weiser have revealed the reorientational motion of the H_i^+ center, and from the stress-induced alignment, its diffusivity at this low temperature [1]. The stress alignment of H_i^+ has been investigated at additional temperatures to confirm and refine our previous results.

2.4 Diffusivity of hydrogen in In_2O_3

The diffusivity of hydrogen in In_2O_3 can be determined from its in-diffusion and out-diffusion behaviors [46–48]. For in-diffusion experiments, In_2O_3 samples were hydrogenated by annealing in an H_2 ambient at temperatures near 700 K. The diffusion depth of H_i^+ was then determined by mechanically thinning a sample and monitoring the amount of H_i removed as a function of depth using measurements of

the 3306 cm^{-1} IR line. An analysis of the H_i^+ remaining, determined spectroscopically as the sample is thinned, yields the diffusivity.

The elimination of the 3306 cm^{-1} line from a hydrogenated In_2O_3 sample by thermal annealing in an inert ambient is governed by the out-diffusion of H_i^+ [46, 47]. Fick's second law [Eq. 2.1] has been used to model the time dependence of the decay of the 3306 cm^{-1} line as a function of the annealing temperature. A fit of the model to the decay of the H_i^+ IR line upon annealing also yields the diffusivity.

$$\frac{\partial C}{\partial t} = D\frac{\partial^2 C}{\partial x^2} \tag{2.1}$$

The In_2O_3 samples used in these IR absorption experiments were bulk single crystals (Fig. 2.3) grown in an air ambient by the flux method [49] at the Oak Ridge National Laboratory (ORNL) [50]. Samples for mass transport measurements were approximately $3 \times 3 \times 1\ mm^3$ in size. Samples were annealed in sealed quartz ampoules that contained H_2 ($2/3 atm$) to introduce hydrogen. Any additional annealing treatments were performed in a tube furnace in a flowing N_2 ambient.

IR absorption spectra were measured with a Bomem DA.3.16 Fourier transform spectrometer (Fig. 1.4) equipped with a KBr beamsplitter and an InSb detector. For measurements performed at 77 K, samples were cooled in a Helitran cryostat (Fig. 2.4 [51]). The probing light was polarized with a wire grid polarizer that was placed in the IR beam path after the cryostat.

Figure 2.3: In_2O_3 bulk single crystals grown in an air ambient by the flux method at the Oak Ridge National Laboratory (ORNL) by Dr. Lynn Boatner. These crystals were pale yellow in color.

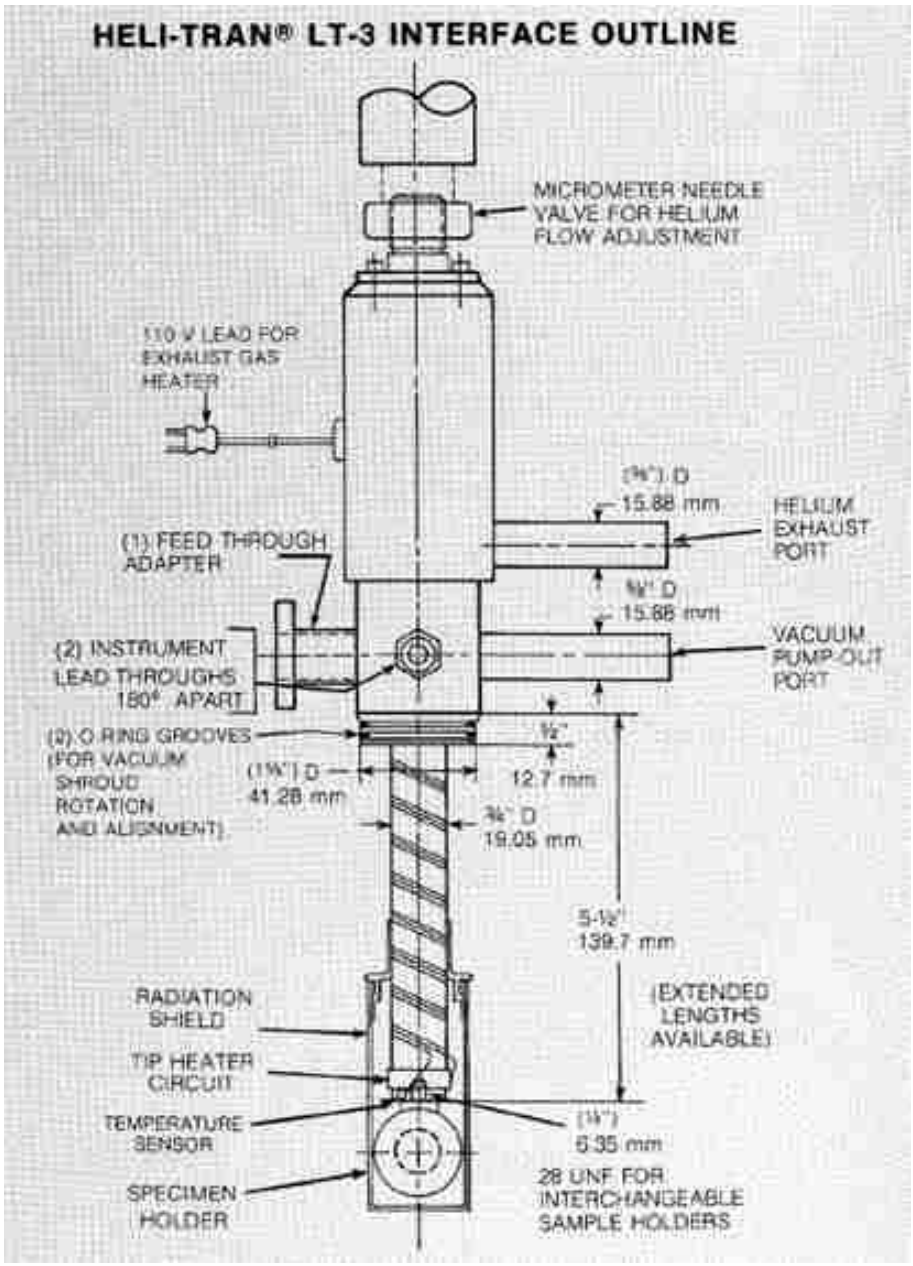

Figure 2.4: Schematic of the Air Products Helitran continuous flow cryostat.

2.5 In-diffusion of hydrogen - fit of profiles

Experiments have been performed to determine the in-diffusion profiles of H_i^+ in In_2O_3 samples following anneals in an H_2 ambient. An as-grown sample was initially annealed at 1273 K for 2 h in flowing N_2 to eliminate any H that might be present. There was no IR absorption due either to free carriers or O-H centers in our samples following this treatment. This sample was then annealed in a sealed ampoule containing $2/3\,atm$ of H_2 for 1 h at a temperature near 723 K to introduce hydrogen into a thin layer near the sample surface.

A thickness of 0.1 mm was lapped from one surface of the sample to completely remove H from that surface. For the other surface, layers were removed successively by lapping and polishing to measure the H_i^+ depth profile. The sample thickness was measured with a micrometer as the sample was thinned in small steps. IR spectra [Figs. 2.5 (a) and 2.6 (a)] were measured to monitor the O-H vibrational absorption at $3306\,cm^{-1}$ as layers were removed.

The integrated absorbance, $A(l)$, of the $3306\,cm^{-1}$ line assigned to H_i^+ decreased as the sample was thinned as is shown in Figs. 2.5 (b) and 2.6 (b). To determine D_H, the diffusivity of H_i^+ at the in-diffusion temperature, a Mathematica program was used to fit these data with the integral of a complementary error function vs. the thickness, l, of the layer removed [Eq. 2.2]

$$A\left(l\right) = A_{max} \int_{l}^{\infty} erfc\left[\frac{x}{2\sqrt{D_H t}}\right] dx. \tag{2.2}$$

The diffusivities determined for H_i^+ at 723 and $698\,K$ in this way are listed in Table. 2.1.

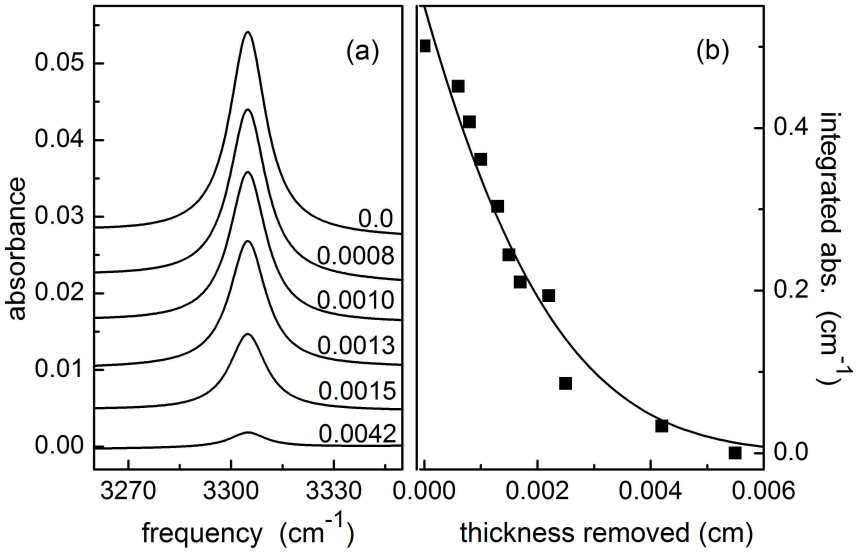

Figure 2.5: (a) IR absorption spectra ($T = 77\,K$, resolution $= 1\,cm^{-1}$) for an In_2O_3 sample that had been hydrogenated by an anneal in an H_2 ambient at $698\,K$ for $1\,h$. The sample was then sequentially thinned by lapping and polishing the front surface. The thickness removed in each thinning step is shown in cm. (b) A fit of the integral of a complementary error function to the area of the $3306\,cm^{-1}$ line vs. the thickness removed by each thinning step.

$T\,(K)$	$D_H\,(10^{-9}\,cm^2/s)$
723	1.0 ± 0.2
698	1.1 ± 0.2
673	0.31 ± 0.1
648	0.14 ± 0.1
623	0.28 ± 0.1
598	0.034 ± 0.01
573	0.025 ± 0.02

Table 2.1: Diffusivity of H_i^+ determined from measurements of its in-diffusion (723 and $698\,K$) and out-diffusion ($673 - 573\,K$) behaviors at the temperatures listed.

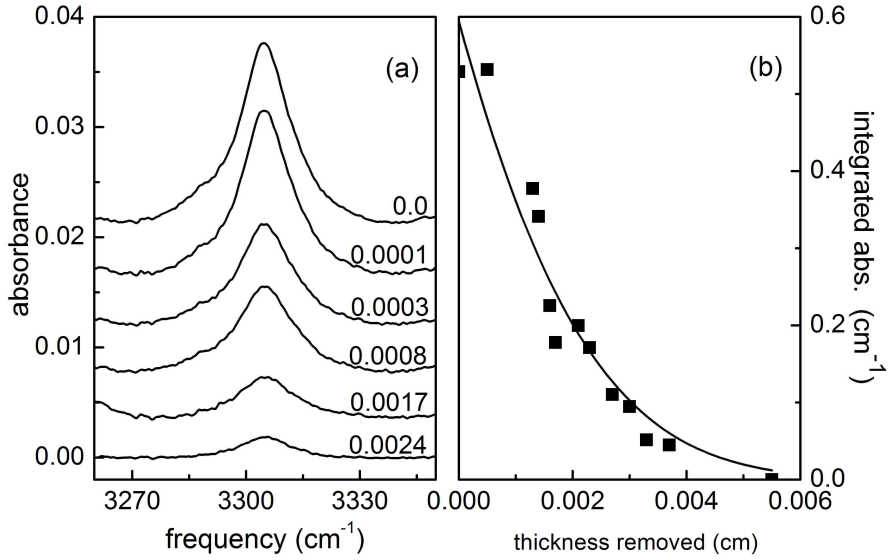

Figure 2.6: (a) IR absorption spectra ($T = 77\,K$, resolution $= 1\,cm^{-1}$) for an In_2O_3 sample that had been hydrogenated by an anneal in an H_2 ambient at $723\,K$ for $1\,h$. The sample was then sequentially thinned by lapping and polishing the front surface. The thickness removed in each thinning step is shown in cm. (b) A fit of the integral of a complementary error function to the area of the $3306\,cm^{-1}$ line vs. the thickness removed by each thinning step.

2.6 Out-diffusion of hydrogen - modeling and fit of profile

Once a thin hydrogenated layer in In_2O_3 has been produced by an anneal in an H_2 ambient, its subsequent elimination by thermal annealing in an inert ambient is governed by the out-diffusion of the H_i^+ center [46, 47]. Spectra of the $3306\,cm^{-1}$ line are shown in Figs. 2.7 (a), 2.8 (a), and 2.9 (a) for samples initially hydrogenated by annealing in an H_2 ambient ($1\,h$ at $723\,K$). Results are shown for increasing annealing times at $T = 673, 648$, and $598\,K$. The integrated absorbance of the $3306\,cm^{-1}$ line vs. the annealing time at $673, 648, 598\,K$ are shown in Figs. 2.7

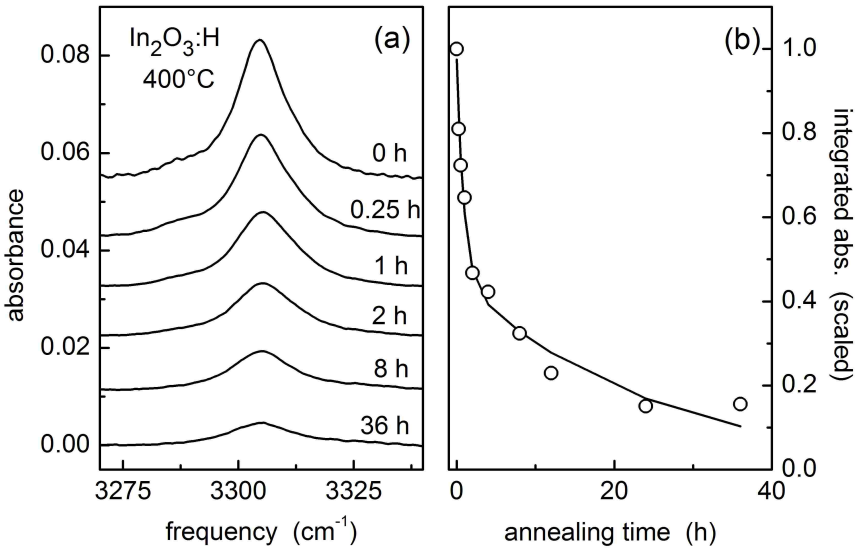

Figure 2.7: (a) IR absorption spectra ($T = 77\,K$, resolution $= 1\,cm^{-1}$) for an In_2O_3 sample that had been hydrogenated by an anneal in an H_2 ambient at $723\,K$ for $1\,h$. The sample was then annealed at $673\,K$ in flowing N_2 for the times shown. (b) The integrated absorbance of the $3306\,cm^{-1}$ line vs. the annealing time in flowing N_2 (divided by its initial value). The line shown is a guide to the eye.

(b), 2.8 (b), and 2.9 (b), respectively. This integrated absorbance, determined experimentally, is proportional to the areal density of the H_i^+ center.

To model the time dependence of the decay of the 3306 cm^{-1} line for annealing in an inert ambient, Mathematica was used to numerically solve the differential equation giving by Fick's Second Law [Eq. 2.1] . The depth profile for the concentration of the H_i^+ center, with an in-diffusion depth determined by our experimental study of the in-diffusion profile of H_i^+, is the starting point for a model of the out-diffusion behavior of H_i^+.

The starting in-diffusion profile was taken to have the functional form: $erfc\left[\frac{x}{2\sqrt{D_H t}}\right]$.

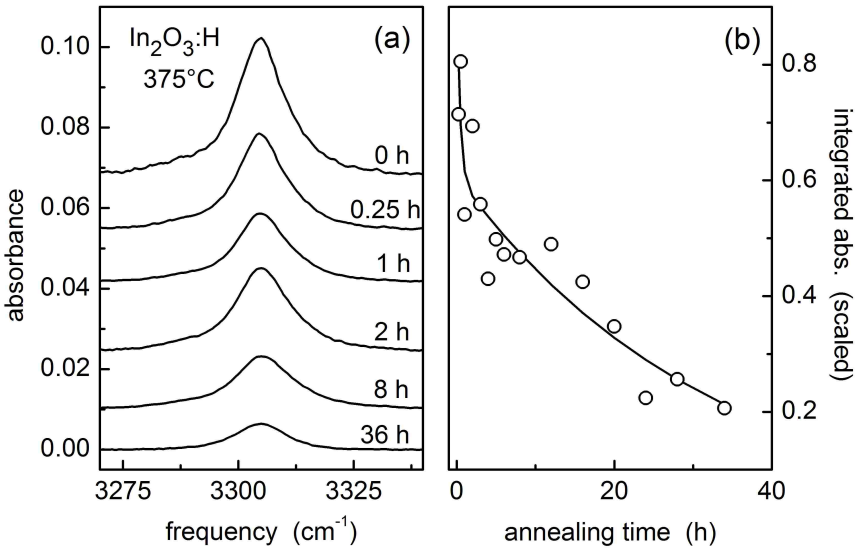

Figure 2.8: (a) IR absorption spectra ($T = 77\,K$, resolution $= 1\,cm^{-1}$) for an In_2O_3 sample that had been hydrogenated by an anneal in an H_2 ambient at $723\,K$ for $1\,h$. The sample was then annealed at $648\,K$ in flowing N_2 for the times shown. (b) The integrated absorbance of the $3306\,cm^{-1}$ line vs. the annealing time in flowing N_2 (divided by its initial value). The line shown is a guide to the eye.

The amplitude of the concentration profile was determined from the integrated absorbance of the $3306\,cm^{-1}$ line measured for a sample following its initial hydrogenation treatment and a calibration of the absorption strength of the $3306\,cm^{-1}$ line determined previously [40].

A numerical solution of Fick's Second Law yields the calculated depth profiles shown in Fig. 2.10 (a) for increasing annealing times. A Mathematica program for performing this fit is shown in the Appendix. The boundary conditions used in solving Fick's Second Law are given by,

$$\begin{aligned} y[0,x] = 3.34((Erfc[\frac{x}{0.00386}] - e^{-100000x}) \times (1 - e^{-1000(x_2-x)}) \\ +(Erfc[\frac{x_2 - x}{0.00386}] - e^{-100000(x_2-x)}) \times (1 - e^{-1000x})) \end{aligned} \tag{2.3}$$

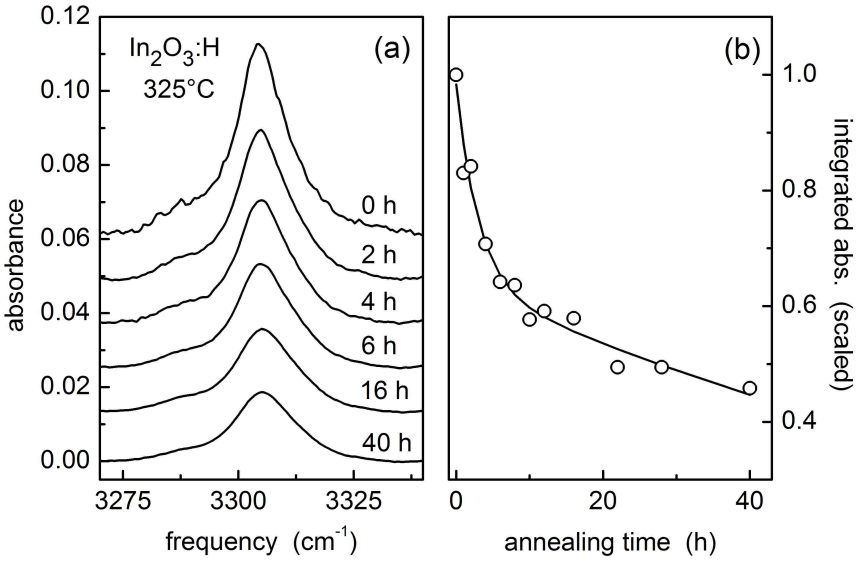

Figure 2.9: (a) IR absorption spectra ($T = 77\,K$, resolution $= 1\,cm^{-1}$) for an In_2O_3 sample that had been hydrogenated by an anneal in an H_2 ambient at $723\,K$ for $1\,h$. The sample was then annealed at $598\,K$ in flowing N_2 for the times shown. (b) The integrated absorbance of the $3306\,cm^{-1}$ line vs. the annealing time in flowing N_2 (divided by its initial value). The line shown is a guide to the eye.

$$y[t,0] = 0, y[t,x_2] = 0 \tag{2.4}$$

Here, $y[0,x]$ is the starting concentration profile with the coefficients of $erfc$ function determined by the in-diffusion profile. To achieve the thin hydrogenated layers at both sides of the sample introduced by the anneal in H_2 ambient, two exponential functions were used to ensure the concentration is zero at both boundaries and is rapidly declining after the thin hydrogenated layers. $y[t,0] = 0 = y[t,x_2]$ means both sides of the sample had zero concentration during the out-diffusion process.

To determine the areal density of H_i^+ as a function of the annealing time in our model, the out-diffusion profiles shown in Fig. 2.10 (a) were integrated numerically over the thickness of the sample to yield the decay of the H_i^+ areal density shown

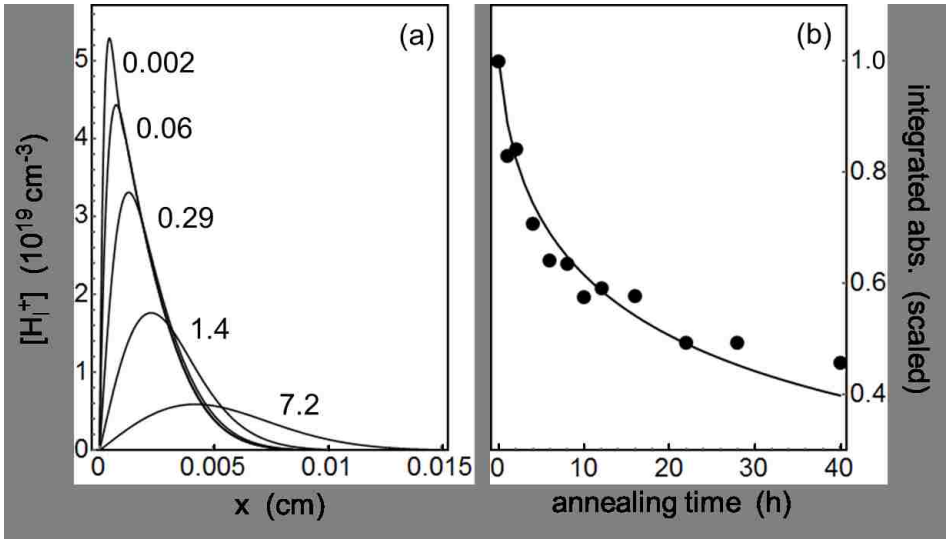

Figure 2.10: (a) H concentration profiles determined numerically for a sample hydrogenated initially in an H_2 ambient at $723\,K$ and subsequently annealed for the times shown (in hours) in an N_2 ambient at $673\,K$ to outdiffuse H. (b) Model results for the areal density of $H_i{}^+$ in In_2O_3 vs the post-hydrogenation annealing time in an inert N_2 ambient (divided by its initial value) are shown by the line. The experimental integrated absorbance of the $3306\,cm^{-1}$ line vs. the annealing time in flowing N_2 is shown by the filled circles.

by the line in Fig. 2.10 (b).

The time dependence of the integrated absorbance of the $3306\,cm^{-1}$ line upon annealing could be fit well by our out-diffusion model, as shown in Fig. 2.10 (b), for an annealing temperature of $673\,K$. To perform such a fit, the value of the diffusivity was adjusted to minimize the sum of the squares of the deviations between the measured data and the results of our diffusion model. Error bars were determined from the values of the diffusivity that increased the value of χ^2, which characterized the fit, by 1. Similar fits were performed for a few additional annealing temperatures ($648, 623, 598,$ *and* $573\,K$ are shown in Figs. 2.11 - 2.14 respectively). Values of the diffusivity of $H_i{}^+$ determined in this way and estimated uncertainties are shown in Table 2.1.

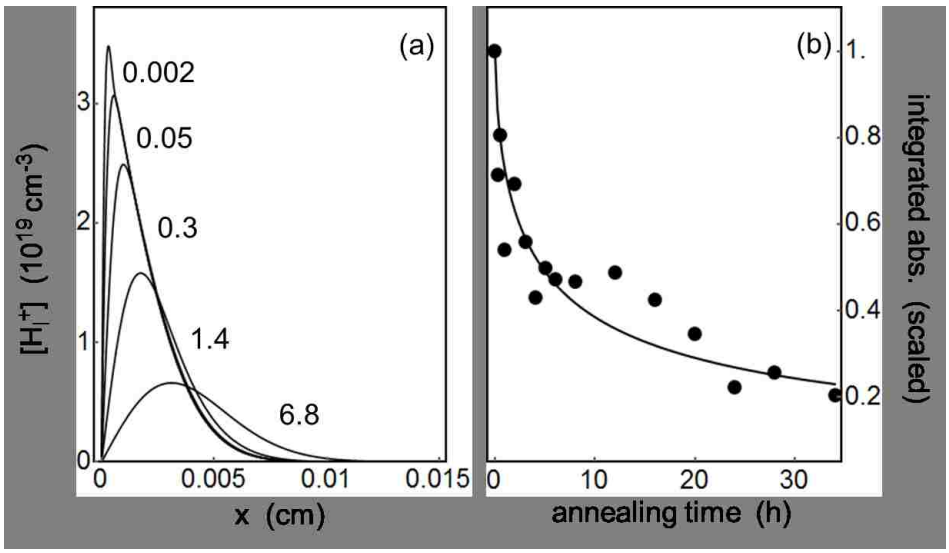

Figure 2.11: (a) H concentration profiles determined numerically for a sample hydrogenated initially in an H_2 ambient at 723 K and subsequently annealed for the times shown (in hours) in an N_2 ambient at 648 K to outdiffuse H. (b) Model results for the areal density of $H_i{}^+$ in In_2O_3 vs the post-hydrogenation annealing time in an inert N_2 ambient (divided by its initial value) are shown by the line. The experimental integrated absorbance of the 3306 cm^{-1} line vs. the annealing time in flowing N_2 is shown by the filled circles.

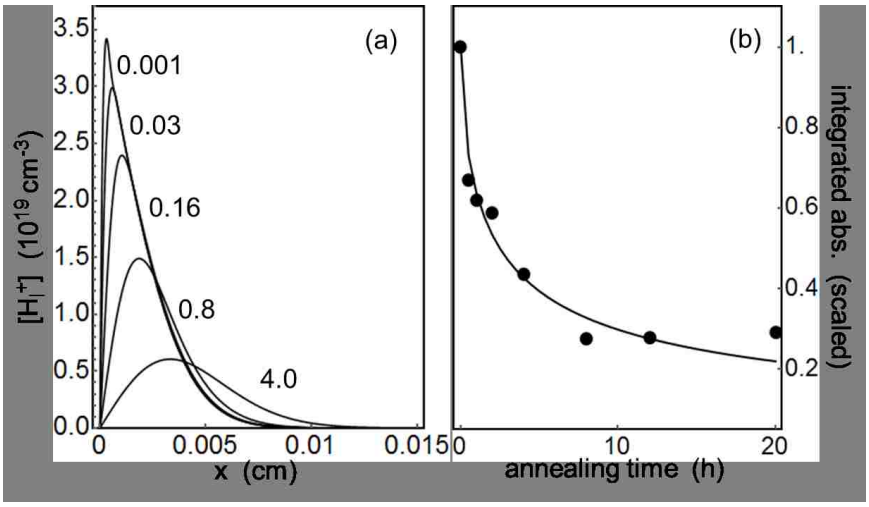

Figure 2.12: (a) H concentration profiles determined numerically for a sample hydrogenated initially in an H_2 ambient at 698 K and subsequently annealed for the times shown (in hours) in an N_2 ambient at 623 K to outdiffuse H. (b) Model results for the areal density of H_i^+ in In_2O_3 vs the post-hydrogenation annealing time in an inert N_2 ambient (divided by its initial value) are shown by the line. The experimental integrated absorbance of the 3306 cm^{-1} line vs. the annealing time in flowing N_2 is shown by the filled circles.

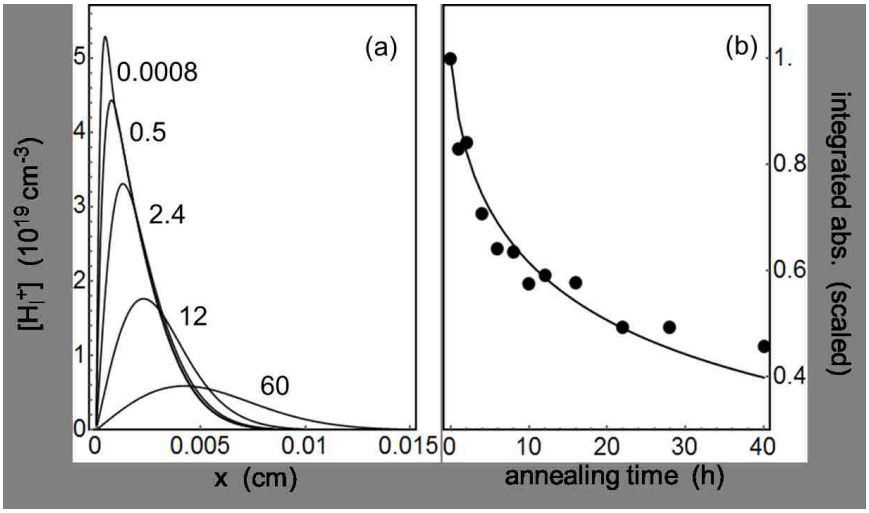

Figure 2.13: (a) H concentration profiles determined numerically for a sample hydrogenated initially in an H_2 ambient at 723 K and subsequently annealed for the times shown (in hours) in an N_2 ambient at 598 K to outdiffuse H. (b) Model results for the areal density of $H_i{}^+$ in In_2O_3 vs the post-hydrogenation annealing time in an inert N_2 ambient (divided by its initial value) are shown by the line. The experimental integrated absorbance of the 3306 cm^{-1} line vs. the annealing time in flowing N_2 is shown by the filled circles.

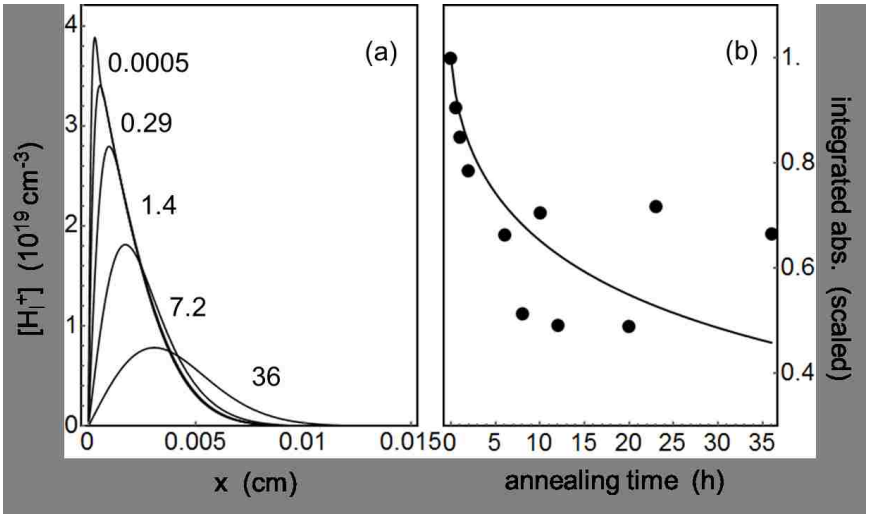

Figure 2.14: (a) H concentration profiles determined numerically for a sample hydrogenated initially in an H_2 ambient at $698\,K$ and subsequently annealed for the times shown (in hours) in an N_2 ambient at $573\,K$ to outdiffuse H. (b) Model results for the areal density of $H_i{}^+$ in In_2O_3 vs the post-hydrogenation annealing time in an inert N_2 ambient (divided by its initial value) are shown by the line. The experimental integrated absorbance of the $3306\,cm^{-1}$ line vs. the annealing time in flowing N_2 is shown by the filled circles.

2.7 Combination of data sets - Diffusivity of H_i^+ for over 11 decades

The diffusivities of H_i^+ in In_2O_3 determined for temperatures near 700 K by mass transport measurements are plotted in Fig. 2.15. The diffusivities determined for temperatures near 160 K by measurements of the H_i^+ jump rate are also shown.

When the H_i doping concentration exceeds the intrinsic carrier concentration, n_i, at the diffusion temperature, an internal electric field that affects the diffusion process is set up by the ionized dopant and its resulting free carriers. The origin of the field comes from the higher mobility of electrons and holes compared to dopant atoms.

Modification can be made to Fick's laws to take account of the electric field ε. For an ionized donor, concentration C, the diffusion equation becomes

$$J = -D_D \frac{\partial C}{\partial x} + B_D \varepsilon C \tag{2.5}$$

D_D and B_D are the diffusion coefficient and mobility of the ionized donor, related by the Einstein equation[46] (assuming a singly ionized donor)

$$\frac{D_D}{B_D} = \frac{kT}{e} \tag{2.6}$$

For the simple case in which all the donors are ionized, this internal electric field ε is contributed by three sets of charged particles: donors, electrons and holes. They each give rise to an electric current due to the effects of normal diffusion and the electric field. These currents are given by [46]

$$j_D = -eD_D \frac{\partial C}{\partial x} + eB_D C\varepsilon \tag{2.7}$$

$$j_n = eD_n \frac{\partial n}{\partial x} + eB_n n\varepsilon \tag{2.8}$$

$$j_p = -eD_p \frac{\partial p}{\partial x} + eB_p p\varepsilon. \tag{2.9}$$

And since there is no net current flow in the crystal,

$$j_D + j_n + j_p = 0 \tag{2.10}$$

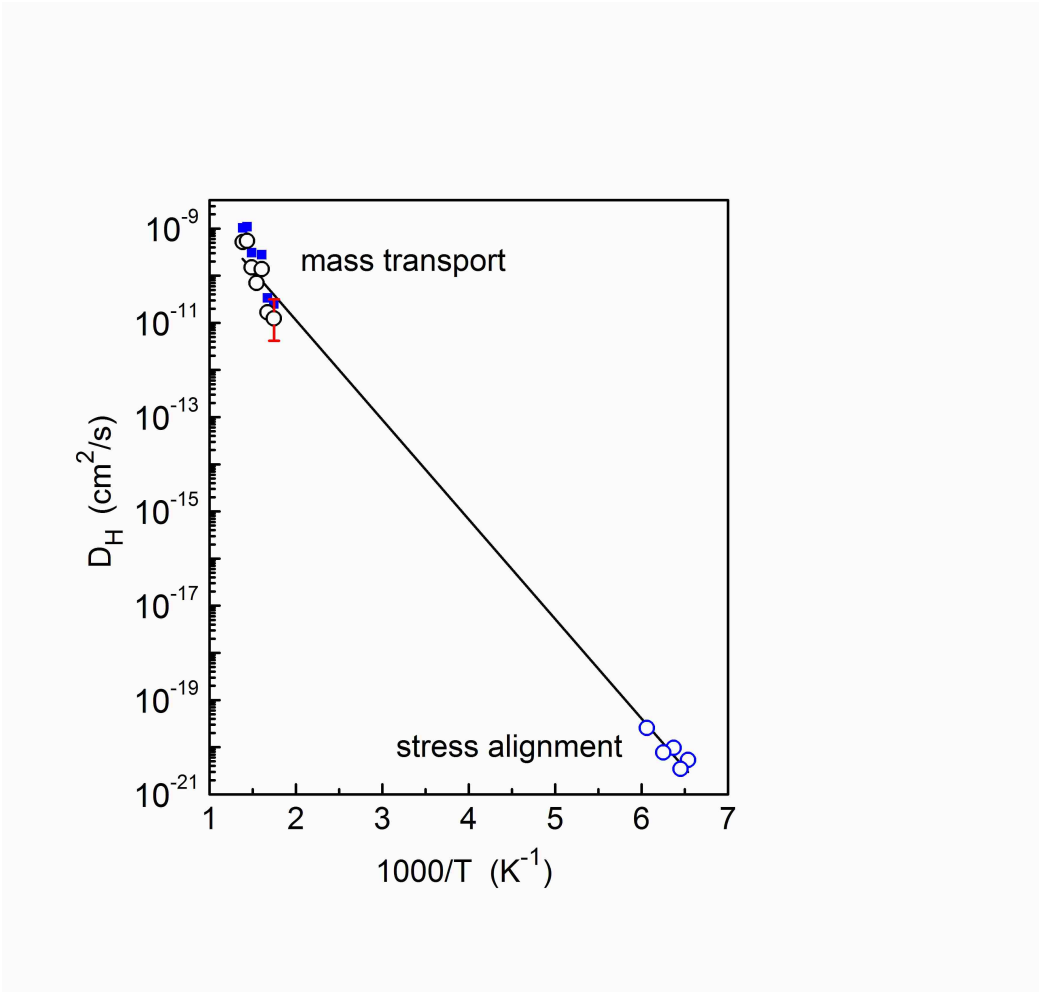

Figure 2.15: The diffusivity plotted vs. $1000/T$ for the interstitial hydrogen shallow donor center in In_2O_3. The filled squares near $700\,K$ show the diffusivity of H_i^+ determined from the in-diffusion and out-diffusion of H_i^+, as measured. The open circles near $700\,K$ show the diffusivity of H_i^+ corrected to account for the enhancement of the diffusivity created by the electric field that arises from H_i^+ and its associated free electrons.

Substituting into Eq. 2.10 from Eqs. 2.7 to 2.9 and solving for ε gives [46]

$$\varepsilon = \frac{kT}{e} \cdot \frac{B_D \frac{\partial C}{\partial x} - B_n \frac{\partial n}{\partial x} + B_p \frac{\partial p}{\partial x}}{B_D C + B_n n + B_p p} \tag{2.11}$$

This internal electric field will be largest when the crystal is strongly n-type ($n \simeq C$ and $p \simeq 0$), so that Eq. 2.11 becomes

$$\varepsilon = \frac{kT}{e} \cdot \frac{\frac{\partial C}{\partial x}\left(B_D - B_n\right)}{C\left(B_D + B_n\right)}. \tag{2.12}$$

Since $B_n \gg B_D$, Eq. 2.12 simplifies to

$$\varepsilon = -\frac{kT}{e} \cdot \frac{1}{C} \frac{\partial C}{\partial x} \tag{2.13}$$

which shows that the built-in field is proportional to the concentration gradient. The flux of donor atoms is given by the modified diffusion equation (Eq. 2.5). Combining Eq. 2.13 and Eq. 2.5 yields,

$$J = -D_D \frac{\partial C}{\partial x} - \frac{kT}{e} \cdot B_D \frac{C}{x} \tag{2.14}$$

Replacing B_D with D_D by Einstein's relation, (Eq. 2.6), gives the result [46]

$$J = -2D_D \frac{\partial C}{\partial x} \tag{2.15}$$

So this built-in field can enhance the diffusivity of the dopant that is causing the field by a maximum factor of two, when the doping concentration C is far greater than the intrinsic carrier concentration so that $n \simeq C$.

As-grown crystals of In_2O_3, similar to those used for our experiments on the H_i^+ center under stress, were found to have high resistivity [50]. Our previous work showed negligible free-carrier absorption for as-grown In_2O_3 samples, consistent with their high resistivity [40]. We concluded that the H_i^+ centers in these samples were present at modest concentration ($\sim 10^{17}\, cm^{-3}$) throughout the bulk of the sample and that these H_i^+ centers were compensated by other defects that were also present. In this case, the net free electron concentration is small and the diffusivity of H_i^+ is not enhanced by an electric field arising from H_i^+ and its associated free electrons.

In contrast to as-grown In_2O_3, the samples used for our in-diffusion and out-diffusion experiments were deliberately hydrogenated in an H_2 ambient to produce thin, heavily doped layers. Hall measurements made in our previous work [40] showed that the concentration of free electrons introduced intentionally by annealing in an H_2 ambient at a temperature near 723 K is greater than $10^{19}\ cm^{-3}$. In this case, the concentration of free electrons introduced by H_i greatly exceeds the intrinsic carrier concentration for In_2O_3, yielding an increase in diffusivity by a factor of two.

The diffusivity of H_i^+ near 700 K is plotted in Fig. 2.15, as measured, by filled squares. The value of the diffusivity, reduced by a factor of 2, is plotted with open circles to make an estimate of the value of D_H that would be observed in the absence of the field arising from H_i^+ shallow donors and their associated free electrons. If we assume a value of 2 as the effect on the value of diffusivity from the intrinsic field to determine D_H near 700 K, we obtain the following diffusivity for H_i^+ (solid line in Fig. 2.15): [52]

$$D_H = (1.9 \pm 0.8 \times 10^{-7}\ cm^2/s) exp(-0.42 \pm 0.01\ eV/kT) \tag{2.16}$$

If we ignore the possible effect of an internal field on the diffusivity, we obtain an activation energy of $E_A = 0.43 \pm 0.01 eV$ and a prefactor of $D_0 = 4.2 \pm 2 \times 10^{-7} cm^2/s$. The uncertainty in the activation energy for diffusion due to any uncertainty in the effect of an internal electric field on the diffusivity is small because of the 11 decade range over which D_H has been measured.

2.8 Discussion

The structure of the H_i^+ center in In_2O_3 and a mechanism for its diffusion have been investigated by Dr. Beall Fowler with hybrid density functional theory calculations that utilized the CRYSTAL06 code with conditions as stated in refs. [40] and [1]. Our previous work on the H_i^+ center in In_2O_3 predicted the mechanism for a diffusion jump of H_i^+ in In_2O_3 that is shown in Fig. 2.2 (ref. [1]). A low energy AB_{01} site is shown in Fig. 2.2(a). The easiest hydrogen jump is to an equivalent AB_{01} partner site on an adjacent oxygen atom. However, this motion will be back-and-forth and

will not give rise to long-range diffusion. For H_i^+ to diffuse, it must migrate to an AB_{01} site that is external to the inner region of this cluster such as the one shown in Fig. 2.2(c). There are two such sites at a predicted distance of 3.003 $\mathring{A}$ from the initial AB_{01} site [1]. Other AB_{01} sites are more distant and are not considered. A model in which an H_i^+ jump, from the site shown in Fig. 2.2(a) to an AB_{01} site such as the one shown in Fig.2.2(c), is the dominant diffusion mechanism leading to the value for the diffusivity based on the H_i^+ jump rate determined in ref. [53] Sec. III. C.

The diffusion pathway proposed by theory also predicts an activation energy for diffusion that can be compared with experiment. There are 4 inequivalent anti-bonding sites for H bonded to an oxygen atom in In_2O_3 [22, 40]. The site AB_{02} shown in Fig. 2.2(b) has a predicted energy that is 0.51 eV greater than that of AB_{01}. (The AB_{03} and AB_{04} sites have energies $\sim 0.8\,eV$ greater than that of AB_{01}.) Theory suggests a diffusion process in which H_i^+ moves from the AB_{01} site shown in Fig. 2.2(a) to the metastable site shown in Fig. 2.2(b). From this metastable configuration, H_i^+ [1] can rotate and move to another lowest energy AB_{01} site [Fig. 2.2(c)] to complete a two-step, diffusion jump. The activation energy of $0.42\,eV$ for diffusion found by experiment is close to the energy difference between the AB_{01} and AB_{02} sites for H_i^+ found by theory, supporting this proposed mechanism.

The diffusivity of H_i^+ measured with stress-induced alignment experiments near 160 K, when combined with mass-transport measurements of the diffusivity of H_i^+ at 723 K, determines the diffusion constant of H_i^+ for over eleven decades.

Theory (Fig. 2.2) predicts a microscopic mechanism for a diffusion jump and the activation energy for diffusion similar to the results determined experimentally.

Chapter 3

Hydrogen in Ga_2O_3

3.1 Ga_2O_3 properties and applications

β-Ga_2O_3 has a monoclinic structure and is attracting much recent attention as a promising transparent conducting oxide with an ultra-wide band-gap (UWBG) [54–58].

The unit cell of β-Ga_2O_3 is shown in Fig. 3.1 [59]. The Ga sites and O sites are color coded. The lattice constants and the angle $\beta = 104^0$ are shown and are the source of low symmetry.

The UWBG semiconductors show promise for device applications with dramatically improved performance [60]. The large band-gap ($4.5 - 4.9\,eV$) of Ga_2O_3 leads to a theoretical breakdown field of $8\,MV/cm$ [55, 59, 61, 62] which has spurred interest in the area of high-power devices [54, 56–58], [63–66]. The Baliga figure of merit for Ga_2O_3 (the figure of merit for power devices, Fig. 3.2 [59]) is at least four times larger than those of GaN and 4H-SiC, making β-Ga_2O_3 an attractive candidate for high-power devices with properties that are improved by orders of magnitude. The ultra-wide band-gap of Ga_2O_3 also opens up opportunities for optoelectronic devices in the deep UV, like solar blind UV photodetectors [58] (semiconductor materials with wide band-gap can be produced and used as "visible-blind" or "solar-blind" detectors that are not affected by daylight), and for devices that can operate in

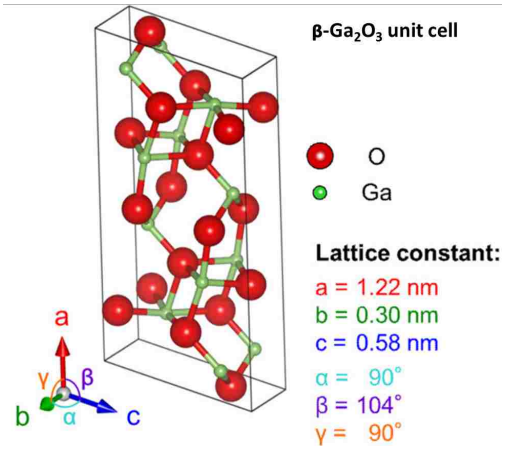

Figure 3.1: Unit cell of β-Ga_2O_3.

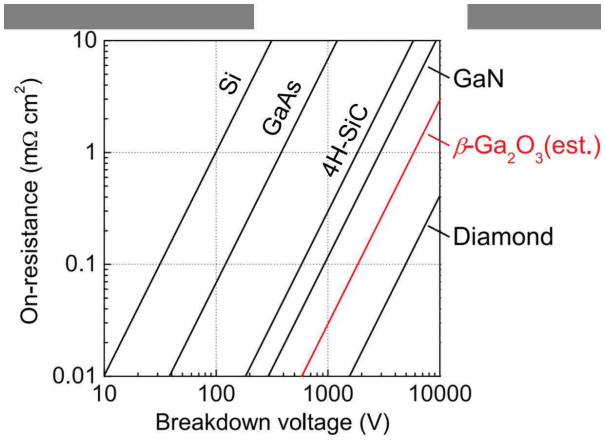

Figure 3.2: Theoretical unipolar performance limits of R_{on} as a function of V_{br} for β-Ga_2O_3 and other major semiconductor power devices.

harsh environments [60].

Another advantage of Ga_2O_3 over the wide-band-gap nitrides is the availability of native single crystal substrates [55].

β-Ga_2O_3 shows unintentional n-type conductivity [67]. While the conventional

wisdom has been that O vacancies can cause this conductivity, theoretical calculations [23, 24] and experiments involving muon spectroscopy [68, 69] predict that O vacancies are not shallow donors and suggest that hydrogen impurities can be a cause of n-type behavior. Both interstitial H and H trapped at an oxygen vacancy are predicted to be shallow donors [23, 24]. Hydrogen can also compensate other defects, like the Ga vacancy (V_{Ga}), that act as deep acceptors [23, 24]. The V_{Ga} defects have been predicted to have a low formation energy and can be passivated by hydrogen to produce a $V_{Ga} - H$ complex with even lower formation energy still and high thermal stability [24]. The interactions of H with V_{Ga} in β-Ga_2O_3 are predicted to give rise to large configurational relaxations of the V_{Ga} defect [24, 70].

This chapter discusses IR absorption studies of hydrogen in Ga_2O_3. Experiments have been performed to determine how different hydrogen centers affect the conductivity of β-Ga_2O_3 and to obtain information about the structure and reactions of hydrogen-related defects.

3.2 O-H spectra - polarization and H-D lines

An IR signature of hydrogen impurities in oxides is one or more vibrational absorption lines in the $3200 - 3500\,cm^{-1}$ range [70] associated with O-H stretch modes (and, for deuterated samples, the corresponding O-D lines in the $2300 - 2600\,cm^{-1}$ range) [41]. A second IR signature occurs when hydrogen acts as a donor whose free electrons give rise to broad free carrier absorption that increases at low frequencies [15, 16].

Furthermore, the polarization properties of the hydrogen vibrational modes in ZnO and SnO_2, for example, have provided valuable information about the structures of the defects that can form [28, 71, 72]. Similarly, the polarization properties of the vibration modes of O-H centers in Ga_2O_3, when combined with theory, help to identify defect structures [70].

Fig. 3.3 shows the sample orientation used in some of our experiments. All of the Ga_2O_3 crystals have a $\left(\bar{2}01\right)$ surface orientation, with [010] and [102] edges, plus

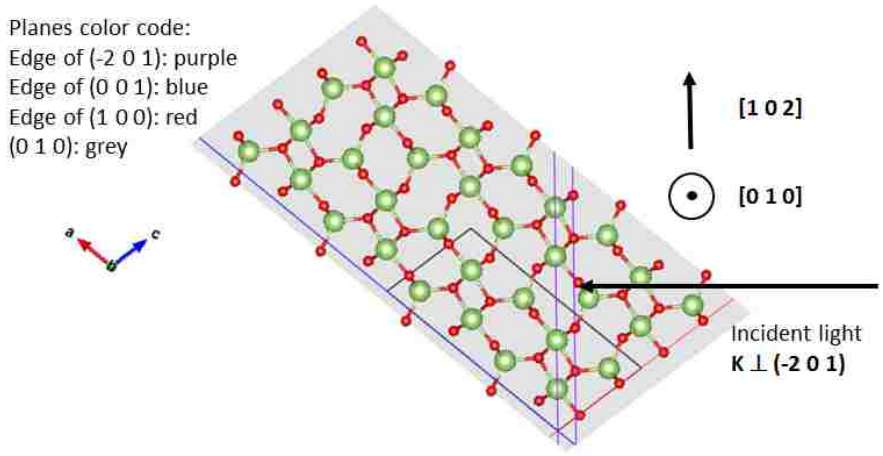

Figure 3.3: Experimental orientation of the samples used in this experiment with sample surface and cleavage planes color coded. Green spheres are Ga atoms and red spheres are oxygen atoms. The β-Ga_2O_3 unit cell is outlined by the black lines and the edges of (001) and (100) planes. This figure was constructed using VESTA - Visualization for Electronic and STructural Analysis and β-Ga_2O_3 crystal structure from Crystallography open database entry 2004987.

(001) and (100) cleavage planes.

IR absorption spectra were measured with a Bomem DA.3.16 Fourier transform spectrometer (Fig. 1.4) equipped with a globar source, a KBr beamsplitter, and an InSb detector. A wire grid polarizer was placed in the IR beam path after the cryostat. Samples were cooled to either 10 or 77 K in an Air Products Helitran cryostat (Fig. 2.4). Subsequent heat treatments were performed in flowing N_2 or Ar.

3.2.1 O-H lines and their polarization properties

In our first experiments performed in collaboration with Phillip Weiser, H and D were introduced into Ga_2O_3 by annealing n-type, single-crystal substrates purchased from the MTI Corporation in an H_2 or D_2 ambient at temperatures above 800^0C.

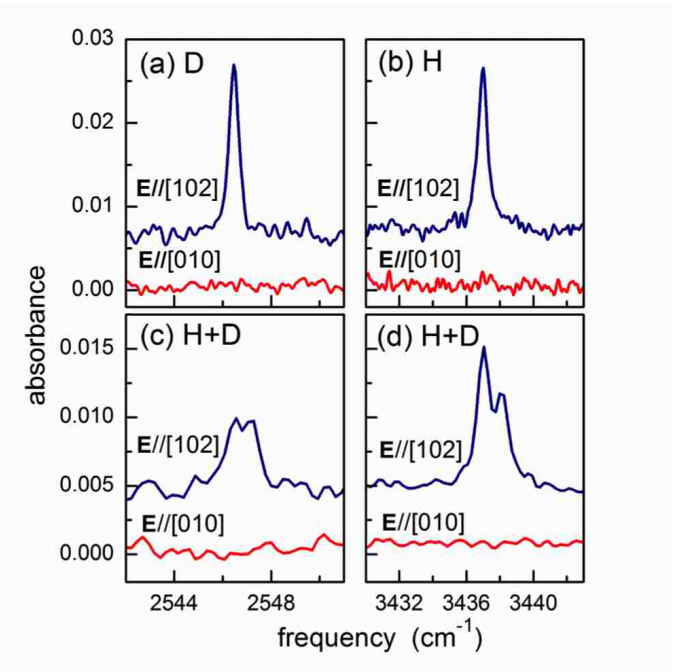

Figure 3.4: Polarized IR absorption spectra obtained at $10\,K$ for the (a) deuterated, (b) hydrogenated, and [(c) and (d)] co-doped samples from MTI.

Fig. 3.4 [70] (a) and (b) show that O-D and O-H vibrational lines are produced at $2546.4\,cm^{-1}$ and $3437.0\,cm^{-1}$, respectively, by the introduction of D and H [70]. These lines are strongly polarized and are seen for the polarization with electric vector $E \parallel [102]$ but not for the polarization with electric vector $E \parallel [010]$.

With the $(\bar{2}01)$ plane as the face of substrates, the polarization with $E \perp (\bar{2}01)$ (i.e. in the $[\bar{1}\ 0\ 2.3]$ direction) could not be thoroughly investigated. Hence these results do not preclude the possibility of absorption in the direction of the incident light $E \parallel [\bar{1}\ 0\ 2.3]$, which would not have been observed [60].

Ga_2O_3 samples can be prepared that contain both H and D to test whether the defects that have been seen contain more than one hydrogen atom. (A defect that contains two H atoms, for example, will have an isotopic sibling that contains both H and D with distinctive vibrational properties that allow it to be identified.)

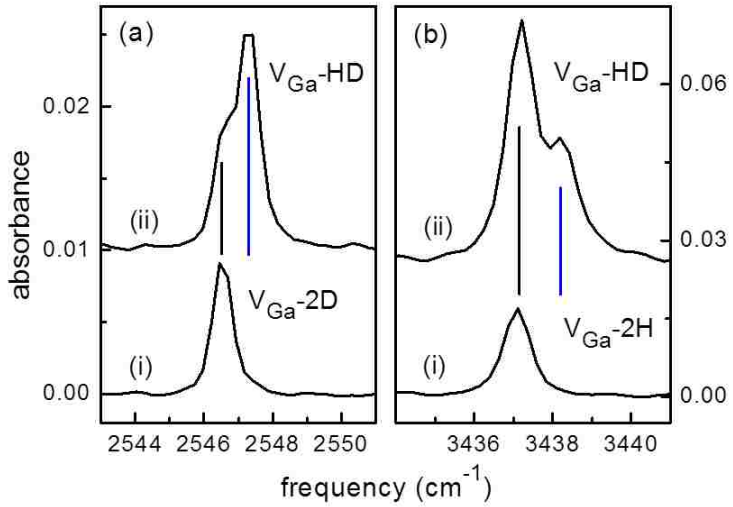

Figure 3.5: Polarized IR absorption spectra ($T = 77\ K$, resolution = $0.5\ cm^{-1}$) for Ga_2O_3 samples from Tamura Corp. annealed in H_2 and D_2 ambients. In panel (a), spectrum(i) is the O-D stretching spectrum for a sample annealed in D_2. In panel (b), spectrum (i) is the O-H stretching spectrum for a sample annealed in H_2. The spectra labeled (ii) in both panels are for a sample annealed in H_2 and D_2.

The spectra shown in Fig. 3.4 (c) and Fig. 3.4 (d) reveal that Ga_2O_3 samples prepared by annealing in a mixture of both H_2 and D_2 do, in fact, show additional new vibrational lines at $3438.2\ cm^{-1}$ for O-H and $2547.1\ cm^{-1}$ for O-D [70]. These new lines are a signature of a defect that contains two identical H (or D) atoms. There are two coupled O-H (or O-D) modes, the first of which is IR active and the second of which is IR inactive. For a defect that contains both H and D, the O-H and O-D modes of the defect become dynamically decoupled and give rise to new vibrational lines for the decoupled oscillators [60]. Furthermore, because the coupled and decoupled modes lie close in frequency, the coupling of the two O-H (or O-D) oscillators must be weak.

N-type Ga_2O_3 samples purchased from the Tamura Corp. also show the same polarization properties ($E \parallel [102]$) and splittings after being annealed in a mixture of H_2 and D_2 at 900^0C followed by an anneal at 400^0C in flowing inert gas [as is shown in Figs. 3.5 (a) and (b)].

3.2.2 Ion implantation and annealing study

The O-H and O-D lines shown in Fig. 3.4, along with a few additional lines, can also be produced by the implantation of protons or deuterons at room temperature [70]. Fig. 3.6 (b) shows results for an n-type Ga_2O_3 sample that is a $0.6\,mm$ thick wafer purchased from the Tamura Corporation that was implanted at room temperature with deuterons with multiple doses and energies up to $280\,keV$ to produce a deuterated layer, $1200\,nm$ thick, with a deuterium concentration of approximately $10^{20}\,cm^{-3}$. Transport of ions in matter (TRIM) simulated concentration profiles are shown in Fig. 3.7.

Introducing deuterium into Ga_2O_3 by the implantation of deuterons produces the $2547\,cm^{-1}$ line that corresponds to the $3437\,cm^{-1}$ O-H line along with several weaker lines at $2518, 2592$ and $2632\,cm^{-1}$ [as is shown in Fig. 3.6 (b)]. Fig. 3.6 (a) shows results for a proton-implanted Ga_2O_3 sample which includes the $3437\,cm^{-1}$ O-H line along with weaker lines at 3392 and $3503\,cm^{-1}$. All of these lines show the same polarization properties and are seen only for ($E \parallel [102]$).

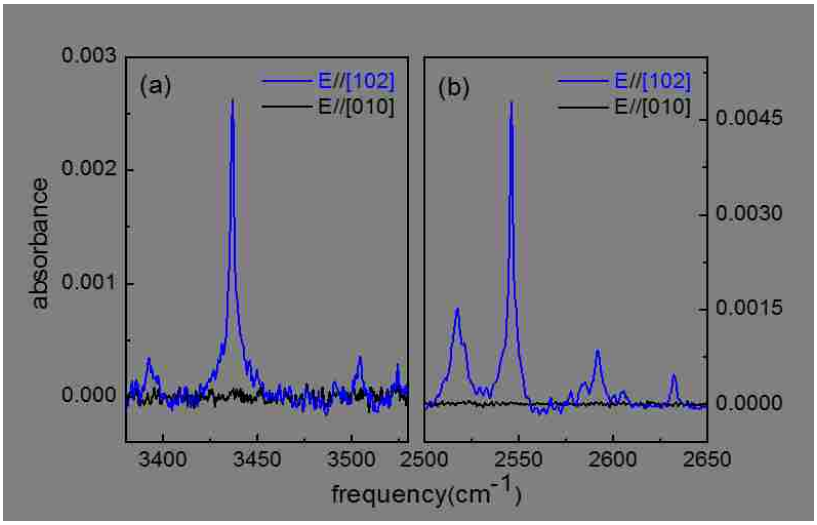

Figure 3.6: Polarized IR absorption spectra obtained at 10 K for a Ga_2O_3 sample from the Tamura Corp. that had been implanted at room temperature with (a) protons or (b) deuterons. Blue spectra were obtained with $E \parallel [102]$, the black null spectra with $E \parallel [010]$.

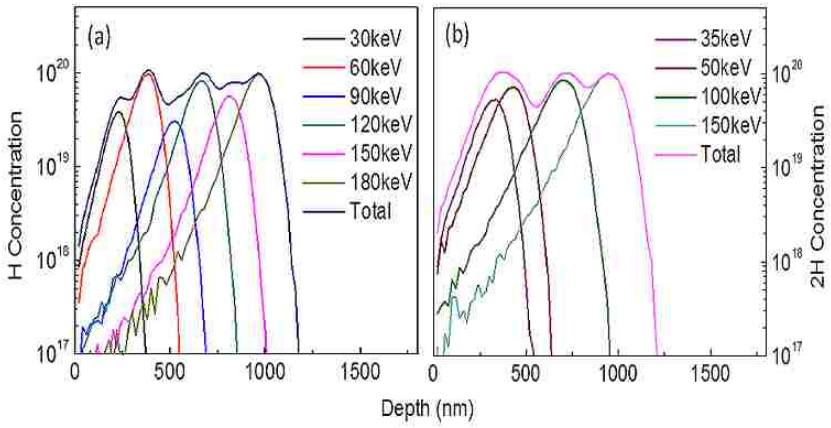

Figure 3.7: Transport of ions in matter (TRIM) simulated concentration profiles of multi-energy proton (a) and deuteron (b) implanted Ga_2O_3 samples purchased from the Tamura Corp. provided by Stephen J. Pearton, Dept. of Materials Science and Engineering, University of Florida.

Fig. 3.8 (a) shows that the dominant line at 2547 cm^{-1} increased in intensity when the D-implanted sample was annealed at 400^0C and other weaker features in the spectrum disappeared. During further annealing (at 500 and 600^0C), several weaker lines at $2535, 2542, 2639, 2475$ and 2531 cm^{-1} were produced, all of which disappeared when the sample was annealed at 1000^0C. Similar behavior was seen in the H-implanted sample as well [as is shown in Fig. 3.8 (b)]. Ga_2O_3 can also be implanted with both H and D. Fig. 3.9 (a) (blue spectrum) shows the O-H stretching region of the H+D-implanted sample and Fig. 3.9 (b) (blue spectrum) shows the O-D stretching region of the same sample. The black dotted spectra in Fig. 3.9 show results for (a) H-implanted and (b) D-implanted samples. Unfortunately, the co-implanted samples did not show resolved lines for defects that contained both H+D. We suspect that the implanted profiles did not lie exactly at the same depths.

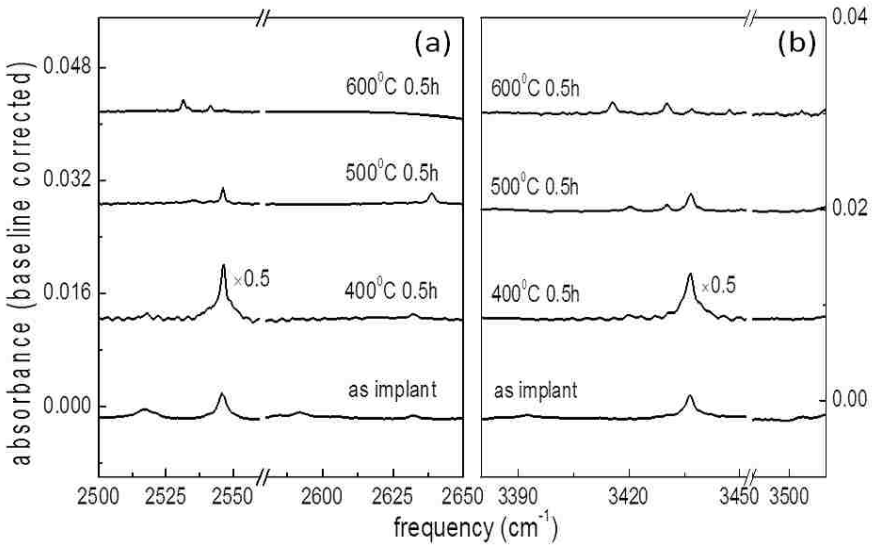

Figure 3.8: Polarized IR absorption spectra obtained at 10 K for a Ga_2O_3 sample from the Tamura Corp. that had been implanted at room temperature with (a) deuterons and (b) protons. Effects of annealing at 400, 500 and 600^0C are shown. Spectra were obtained with $E \parallel [102]$.

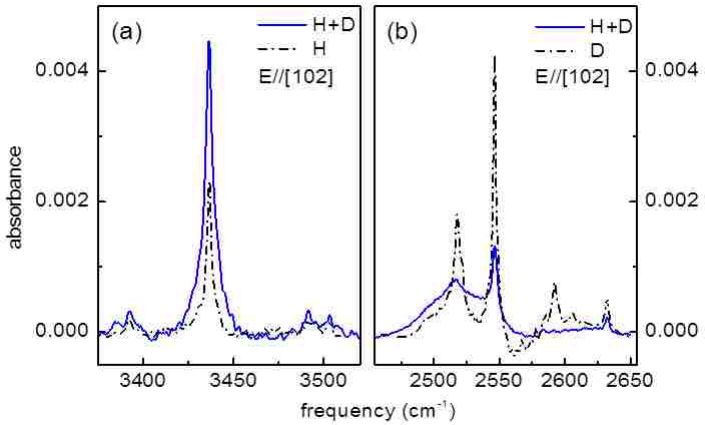

Figure 3.9: Polarized IR absorption spectra obtained at 10 K for a Ga_2O_3 sample from the Tamura Corp. that had been implanted at room temperature with both protons and deuterons (blue). The black dotted lines are samples that had been implanted with just (a) protons or (b) deuterons.

3.2.3 Thinning experiment

Experiments have been performed to determine the hydrogenated layer thickness of a Ga_2O_3 sample following an anneal in a D_2 ambient at temperatures above 800^0C. A n-type Ga_2O_3 sample that is a $0.68\,mm$ thick wafer purchased from the Tamura Corp. was deuterated in a D_2 ambient at 900^0C for $1\,h$ followed by a subsequent anneal in flowing Ar at 400^0C for $0.5\,h$ to increase the intensity of the $2546.4\,cm^{-1}$ line. A thickness of $0.1\,mm$ was lapped from one surface of the sample to completely remove D from that surface (as is shown in Fig. 3.10). For the other surface, layers were removed successively by lapping and polishing to measure the $D_i{}^+$ depth profile. The sample thickness was measured with a micrometer as the sample was thinned in small steps. IR spectra [Fig. 3.11 (a)] were measured to monitor the O-D vibrational absorption at $2546.4\,cm^{-1}$ as layers were removed.

The integrated absorbance, $A(l)$, of the $2546.4\,cm^{-1}$ line decreased as the sample was thinned as is shown in Fig. 3.11 (b). To determine the thickness of the deuterated layer, D_D, a Mathematica program was used to fit these data with the integral of a completary error function vs. the thickness, l, of the layer removed [Eq. 3.1]. The fit result yields a deuterium in-diffusion depth of $L_D = 2\sqrt{D_D t} = 0.0030 \pm 0.0005\,cm$ for an annealing temperature of 900^0C for $1\,h$. These results yield an effective diffusivity of $D_D\,(900^0C) = (6.3 \pm 2.1) \times 10^{-10}\,cm^2/s$. (This is 200 times smaller than the diffusivity of H in TiO_2 at the same temperature.)

$$A\,(l) = A_{max} \int_l^\infty erfc\left[\frac{x}{2\sqrt{D_D t}}\right] dx. \tag{3.1}$$

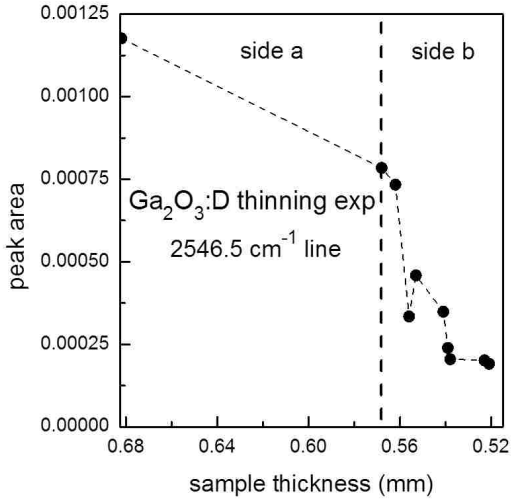

Figure 3.10: A selection of area of the $2546.4\,cm^{-1}$ line vs. the thickness (mm) removed by each thinning step for a Ga_2O_3 sample that had been deuterated in a D_2 ambient at 1173 K for 1 h followed by a subsequent anneal in flowing Ar at 673 K for 0.5 h.

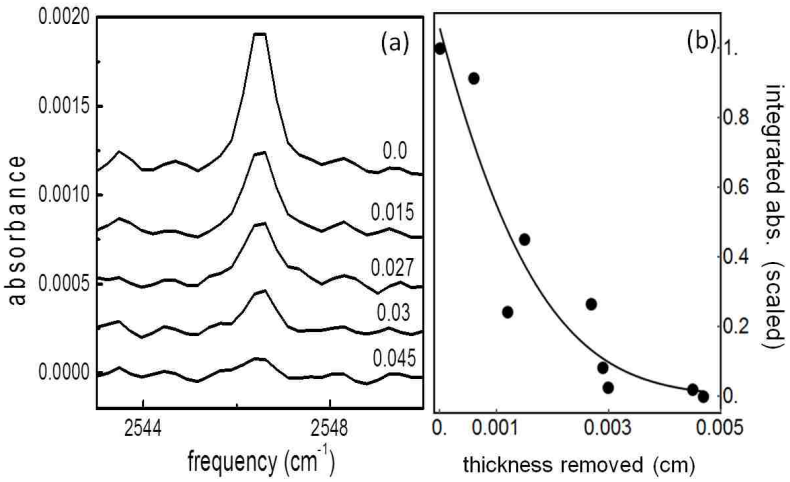

Figure 3.11: (a) A selection of IR absorption spectra ($T = 77\,K$, resolution $= 0.5\,cm^{-1}$) for a Ga_2O_3 sample that had been deuterated in an D_2 ambient at $1173\,K$ for $1\,h$ followed by a subsequent anneal in flowing Ar at $673\,K$ for $0.5\,h$. The thickness removed (l) in each thinning step is shown in cm. (b) A fit of the integral of a complementary error function to the area of the $2546.4\,cm^{-1}$ line vs. the thickness removed by each thinning step.

3.3 V_{Ga}-H_2 center - Fowler Model

β-Ga_2O_3 has a complex monoclinic crystal structure [Fig. 3.12 (a)] [73, 74]. There are two inequivalent Ga sites and three inequivalent oxygen sites. Ga(1) and Ga(2) are tetrahedrally and octahedrally coordinated, respectively. O(1) and O(2) are three-fold coordinated and O(3) is four-fold coordinated.

There are a variety of defects that can exist in the complex β-Ga_2O_3 structure [75–78], and hydrogen can interact with many of them. As a result, there are many possible configurations for interstitial H and for H complexes with native defects such as O or Ga vacancies [60]. The constraints provided by the polarization data and the small line splittings observed in IR spectra so far are a much stronger test of the defect structure than the O-H vibrational frequencies themselves which typically all lie in the vicinity of $3400 - 3500\, cm^{-1}$ [70].

Many potential defect configurations were investigated by W.B. Fowler (Lehigh Univ.) by carrying out calculations using the CRYSTAL06 code [52], choosing density-functional theory (DFT) with a gradient-corrected approximation to the exchange-correlation functional. Details of such calculations can be found in Ref. [70].

The first candidate being considered was interstitial H. From Fig. 3.12 [79], one can see that H_i could attach to one of two opposing sites on O(1) or O(2), or one of four quasitetrahedral sites on O(3). Several of these have their O-H dipole perpendicular to [010] and therefore are candidates for single O-H defects.

The next logical candidate as a host for O-H dipoles in metal oxides is a metal vacancy; in this case, the Ga vacancy. There is both experimental [80] and theoretical [24] support for the common existence of Ga vacancies in Ga_2O_3. Furthermore, the V_{Ga}-H complex has been predicted to have low formation energy [24]. The structures of unrelaxed (a) and relaxed [(b) and (c)] V_{Ga} defects are shown in Fig. 3.13.

After eliminating several potential Ga-vacancy-related two-H defect structures, the defect that satisfies all of the experimental conditions and constraints is shown in Fig. 3.14. It involves two H trapped in a relaxed $Ga(1)_{23}$ vacancy [as is shown in Fig.

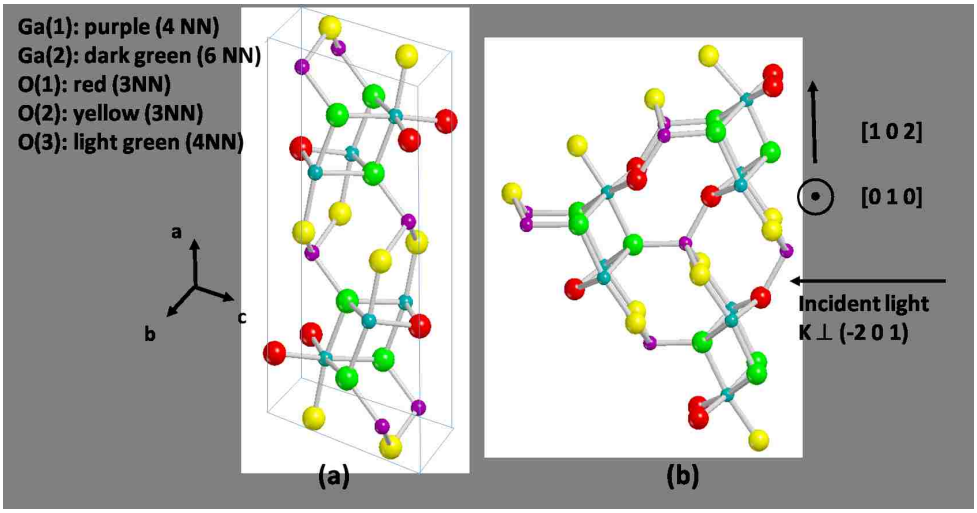

Figure 3.12: (a) The unit cell of β-Ga_2O_3. The inequivalent sites are color coded as follows: Ga(1), purple; Ga(2), dark green; O(1), red; O(2), yellow; and O(3), light green. (b) Experimental orientation of the samples used in this experiment. These and subsequent figures were constructed using MOLDRAW45 (`http://www.moldraw.unito.it`) and POV-Ray (`http://povray.org`).

3.13 (b)]. As shown in Fig. 3.14, the two O-H dipoles are equivalent, antiparallel, and weakly coupled, with zero [010] projections and large [102] projections. This defect is also the most stable (lowest energy) of all the combinations considered by Fowler by $\approx 0.6\,eV$. The computed harmonic frequencies for the two local modes shown in Fig. 3.14 are $3738.0\,cm^{-1}$ for the odd (observed) mode and $3739.0\,cm^{-1}$ for the even (unobserved) mode. This leads to an emergent mode when one H is replaced by a D of $3738.7\,cm^{-1}$, displaced from the original mode by $0.7\,cm^{-1}$. This compares well with the experimental shift of $1.2\,cm^{-1}$.

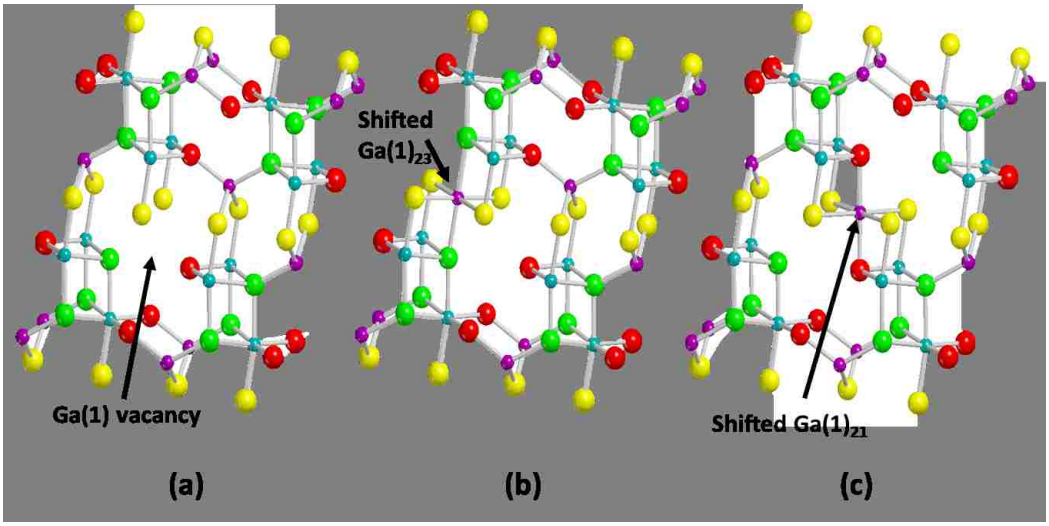

Figure 3.13: Possible Ga(1) vacancy sites: (a), unrelaxed; (b), neighboring Ga(1) shifted to site with O(2) and O(3) neighbors [$Ga(1)_{23}$]; (c) neighboring Ga(1) shifted to site with O(2) and O(1) neighbors [$Ga(1)_{21}$].

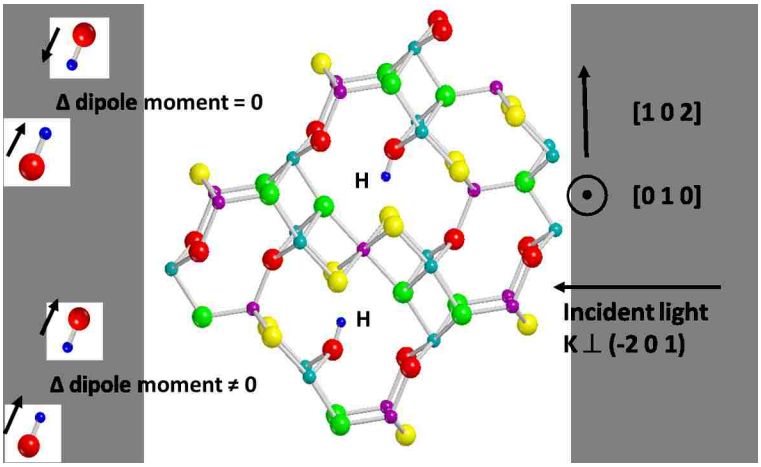

Figure 3.14: Relaxed configuration of $Ga(1)_{23}$ plus two H which satisfies the polarization and coupling constraints for the 3437 cm^{-1} line in hydrogenated Ga_2O_3. The hydrogen motions for the even and odd modes with zero and nonzero transition moments, respectively, are illustrated.

3.4 Hidden hydrogen

In the process of introducing H into Ga_2O_3 and producing the 3437 cm^{-1} center, an interesting phenomenon was observed. A two-step annealing process was found to effectively produce the 3437 cm^{-1} center. And possible candidates were explored to explain this intriguing behavior of hydrogen in Ga_2O_3.

3.4.1 Spectra and annealing (-2 0 1) face

Following an anneal in an H_2 ambient at a temperature of 800^0C or greater, the sample showed either a weak 3437 cm^{-1} line or no such line at all [as is shown in Fig. 3.15 (b), spectrum(i)]. It was not until after a second annealing treatment at 400^0C in flowing N_2 or other inert ambient that the sample showed a strong 3437 cm^{-1} O-H vibrational line [as is shown in Fig. 3.15 (b), spectrum (ii)].

The same behavior was seen in samples that had been deuterated by annealing in a D_2 ambient [as is shown in Fig. 3.15 (a), spectrum(i)]. The second annealing step at 400^0C, Fig. 3.15 (a), spectrum(ii), shows that the second anneal produced the 2547 cm^{-1} O-D vibrational line.

These results show that H is introduced in Ga_2O_3 by the first anneal at $T > 800^0C$ in a form that does not give rise to an observable O-H line for polarization normal to the $(\bar{2}01)$ face of the sample. A second anneal at a temperature near 400^0C transforms this hidden reservoir of H into the defect that gives rise to the 3437 cm^{-1} center [60].

Furthermore, as is mentioned in Section 3.2.2, Ga_2O_3 samples hydrogenated (or deuterated) by the ion implantation of protons (or deuterons) also show interesting hydrogen reactions upon annealing at 400^0C in an inert ambient. Fig. 3.8 (a) shows that annealing a sample at 400^0C that had been implanted with D increases the strength of the 2547 cm^{-1} line by roughly 4 times, suggesting the presence of the same hidden species that is formed in Ga_2O_3 samples annealed in a D_2 ambient. However, in the implanted samples, there are also weaker lines [shown in Fig. 3.8(a)] that disappeared upon the 400^0C anneal which could contribute to the increase in

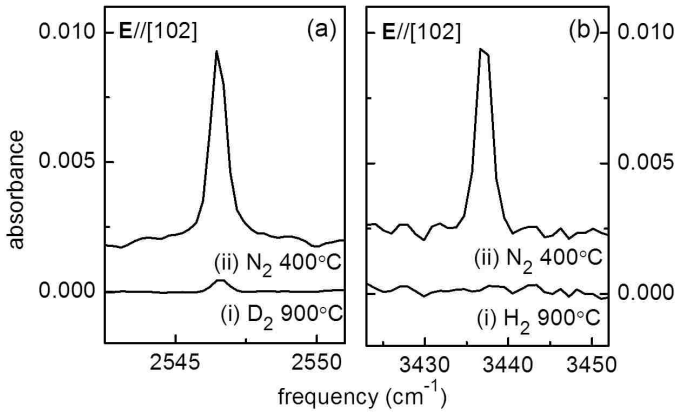

Figure 3.15: IR absorbance spectra for a Ga_2O_3 sample that had received a two step annealing treatment to introduce hydrogen. Spectrum (i) was measured for a sample annealed in an (a) D_2 or (b) H_2 ambient for 1 h at 900^0C. Spectra (ii) in (a) and (b) are for the same sample after a subsequent anneal at 400^0C in flowing N_2.

size of the 2547 cm^{-1} line.

3.4.2 Possible explanations of the hidden H - H_2, H_o, O-H centers perpendicular to (-2 0 1)

There are several possibilities for the hidden form of hydrogen that exists in Ga_2O_3 after the first anneal in H_2 gas at elevated temperatures. Various hydrogen defects in other TCOs have been studied in the past. The following candidates for hidden hydrogen in Ga_2O_3 are suggested by these previous studies. (i) Hydrogen could be introduced in the form of interstitial H_2 molecules whose vibrational modes are not IR active. Hidden H_2 in ZnO was found to serve as a reservoir for H to which H_i could be converted by thermal annealing at 150^0C [25, 30], as is described in Chapter 1 Section 1.3.2. (ii) Hydrogen could also be trapped at an oxygen vacancy (H_o) which is predicted by theory [23] to act as a shallow donor. It has a low vibrational frequency that appears in the spectral region where oxides are highly

absorbing. This is seen in ZnO as well [20, 32]. (iii) There could be O-H centers with transition moments oriented primarily along the direction of the incident light ($E \parallel [\bar{1}\ 0\ 2.3]$), as is mentioned in Section 3.2.1. Such a defect would not have been seen for the polarizations of the probing light that have been used in the experiments described so far.

3.4.3 Hydrogen shallow donors

Data shown in Fig. 3.16 support the candidates, H_i or H_o, as sources of "hidden hydrogen" in Ga_2O_3 samples. Spectrum (i) in Fig. 3.16(a) shows the free-carrier absorption for a Ga_2O_3 sample that was annealed in an H_2 ambient at 1000^0C. The $3437\,cm^{-1}$ O-H line is not present following this annealing treatment. Spectrum (ii) shows that the free-carrier absorption is reduced by a subsequent anneal at 400^0C in an inert ambient. Meanwhile, this second annealing treatment also produces the $3437\,cm^{-1}$ line [spectrum (ii) in Fig. 3.16(b)]. Spectrum (iii) shows that further annealing at 1000^0C in an inert ambient removes the $3437\,cm^{-1}$ center from the sample. The spectra labeled (iv) in Figs. 3.16(a) and (b) show the differences of spectra (i) and (ii) in the same panels. These difference spectra emphasize contributions arising from H rather than from other donors (presumably Sn or Si) that can be present. In Fig. 3.16(a), spectrum (iv), the increase in the broad-absorption at low frequency is due to the free-carrier absorption which is caused by hydrogen in the sample.

These results suggest that an H-related shallow donor introduced by the anneal in H_2 is converted into the $3437\,cm^{-1}$ O-H center by a subsequent anneal at 400^0C in an inert ambient. Interstitial hydrogen (H_i) or hydrogen trapped at oxygen vacancy (H_o) predicted by theory [23] are good candidates for such H-related shallow donors that might serve as a reservoir of hidden hydrogen that can be produced by annealing a Ga_2O_3 sample in an H_2 ambient. However, these results do not eliminate other possibilities (like H_2 molecules) that may also provide a reservoir of hydrogen in our samples that are difficult to observe directly.

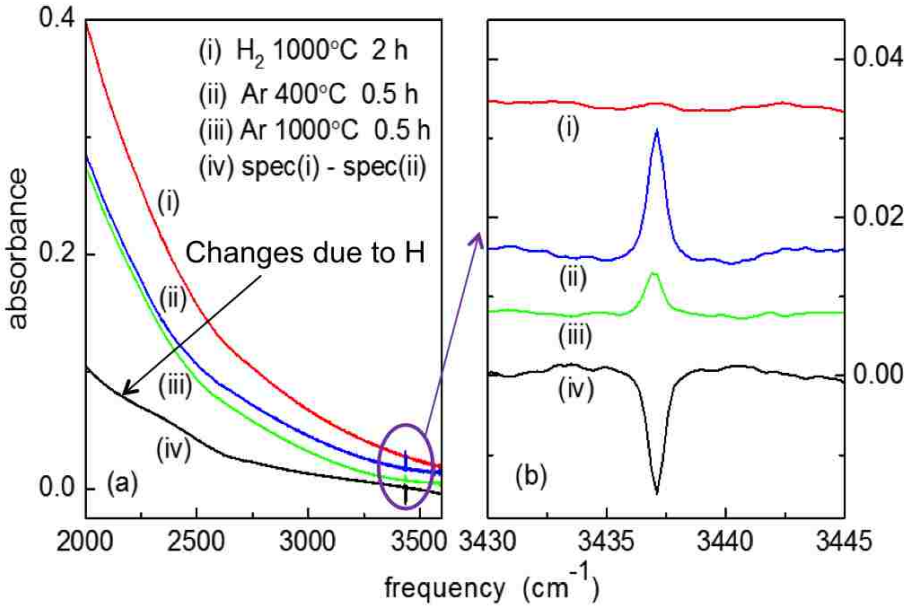

Figure 3.16: IR absorption spectra ($(T = 77\,K)$, resolution $0.5\,cm^{-1}$) for a Ga_2O_3 sample from Tamura Corp. that initially had been hydrogenated by an anneal at 1000^0C. This sample was subsequently annealed in Ar at the temperatures indicated. (a) shows the absorption due to free carriers. (b) shows the $3437 cm^{-1}$ O-H vibrational line that corresponds to the free-carrier data shown in (a)

3.5 Additional hydrogen centers in Ga_2O_3

The $2546.5\,cm^{-1}$ vibrational line is the dominant feature seen in Ga_2O_3 samples deuterated in a D_2 ambient. However, when such a sample was annealed in an inert ambient at elevated temperature ($T > 900^0C$) to remove H or D and then retreated in D_2, several additional IR lines were produced. Fig. 3.17 (a) spectrum (ii) shows O-D lines at 2583.7 and $2632.6\,cm^{-1}$ that were seen (in addition to the $2546.5\,cm^{-1}$ line) for the polarization with $E \parallel [102]$ for a Ga_2O_3 sample that had been deuterated by annealing in D_2 at 900^0C (1h) and then cooled by placing the ampoule on a metal plate at room temperature. The $2632.6\,cm^{-1}$ line was also seen in a sample implanted with deuterons [Fig. 3.6(b)].

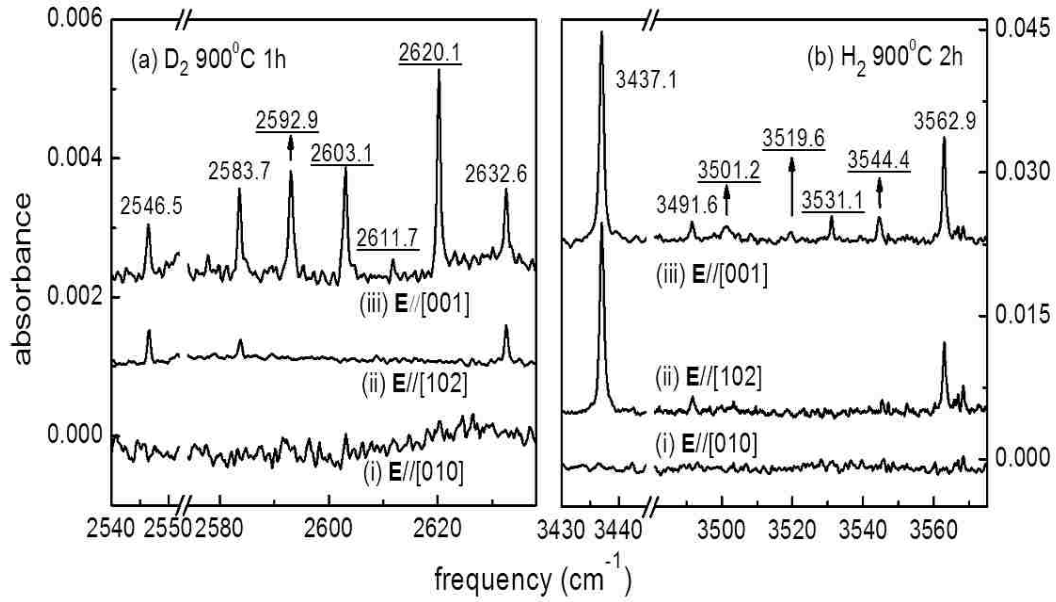

Figure 3.17: Polarized IR absorption spectra (77 K, resolution 0.5 cm^{-1}) for Ga_2O_3 samples from the Tamura Corp. that had been annealed at 900^0C in (a) a D_2 ambient and (b) in an H_2 ambient. Spectrum (i) and (ii) in both panels were measured for a sample mounted on its $(\bar{2}01)$ face for the polarization direction indicated. Spectra (iii) in both panels were measured for the sample mounted on a cleaved (100) surface.

We have performed new experiments with a different sample orientation to access other polarization directions. We attempted to hydrogenate Ga_2O_3 samples from the Tamura Corp. with a (010) face. However, we could not produce hydrogen lines in samples with a (010) face, even after several attempts with high temperature anneals (950^0C) in H_2.

We then investigated a wafer with a $(\bar{2}01)$ face that had been cleaved to produce a (100) planar edge surface [see Fig. 3.18 (b)]. In this case, hydrogen or deuterium could be introduced into the $(\bar{2}01)$ face of the sample, similar to the experiments described in the sections above. The (100) face of the cleaved sample was then

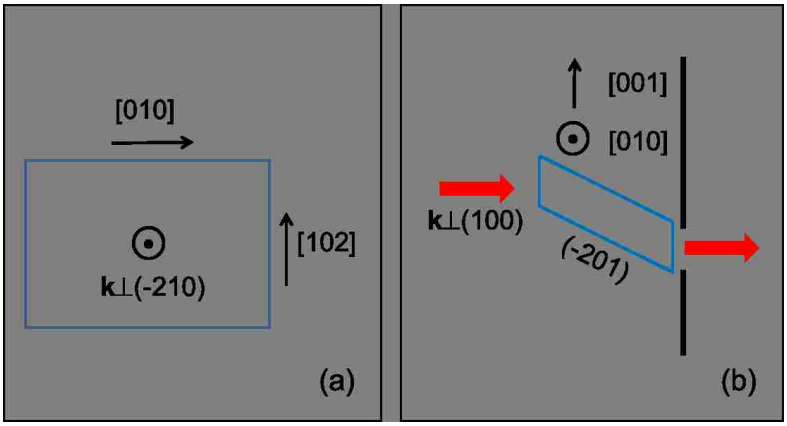

Figure 3.18: (a) Experimental orientation when a sample is measured with light ($\mathbf{k} = [\bar{1}\ 0\ 2.3]$) perpendicular to sample's $(\bar{2}01)$ face. This set up is used in all previous Sections. (b) Experimental orientation used to observe the absorption with transition moment along the direction that is perpendicular to the sample's $(\bar{2}01)$ face. The set up in (b) was achieved by rotating the sample about its [010], so that the electric vector of the incident light had components parallel to $[\bar{1}\ 0\ 2.3]$ and [102] directions.

mounted on a slit with a width of approximately $0.5\,mm$ for an optical transmission measurement with a light propagation direction $\mathbf{k} \perp (100)$ [Fig. 3.18 (b)]. Polarizations with electric field directions $E \parallel [001]$ and $E \parallel [010]$ could be investigated. This sample geometry allowed a polarization direction with a large component normal to $(\bar{2}01)$ (which is $E \parallel [\bar{1}\ 0\ 2.3]$) to be investigated for a sample for which its $(\bar{2}01)$ face had been hydrogenated.

Fig. 3.17 (a) shows data for a Ga_2O_3 sample that had been deuterated by annealing in D_2 at 900^0C (1h) and then cooled by placing the ampoule on a metal plate at room temperature. Spectrum (iii) in Fig. 3.17 (a) is for the [001] polarization direction which we have not yet investigated. In addition to the three lines already seen in the $E \parallel [102]$ polarization, four new IR lines (underlined) are produced. These four new lines must be due to OD centers with their transition moments along the $[\bar{1}\ 0\ 2.3]$ direction [perpendicular to $(\bar{2}01)$ plane].

Fig. 3.17 (b) shows that corresponding results for hydrogenated samples are

Table 3.1: Frequencies of O-H and O-D IR lines seen in hydrogenated and deuterated Ga_2O_3. The ratio of the frequencies of corresponding O-H and O-D centers, $r = \omega_H/\omega_D$, is also shown.

similar, again with four new IR lines, whose frequencies are shown underlined, seen only for the polarization with [001].

The O-H and O-D frequencies for the lines shown in Fig. 3.17 are listed in Table 3.1. The ratio of the O-H and O-D frequencies for corresponding lines, $r = \omega_H/\omega_D$, is $r = 1.35$. This value for r is characteristic of O-H and O-D centers where H and D are bound to a light-mass atom like oxygen [81].

3.5.1 Annealing behavior of the new lines and correlation with free carriers

Figures 3.19 (a) and (b) show the effect of thermal annealing on the O-H and O-D lines in Ga_2O_3. Because the cooling rate of the sealed ampoule after the treatment at 900^0C in H_2 or D_2 ambient is hard to control, the new features with polarization along the [001] direction can be, in some cases, strengthened by a subsequent anneal

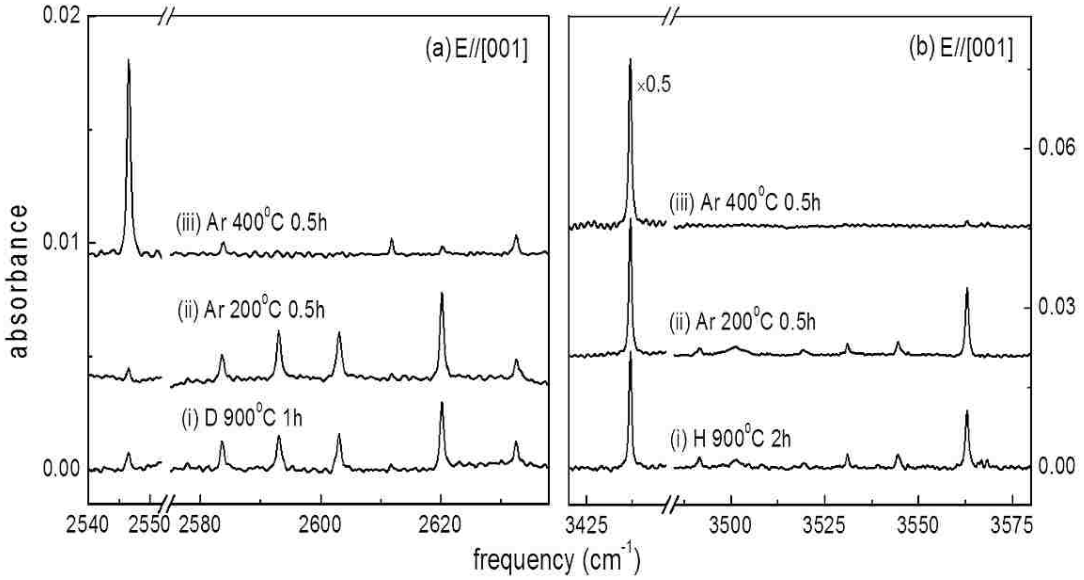

Figure 3.19: IR absorption spectra (77 K, resolution 0.5 cm^{-1}) for Ga_2O_3 samples mounted on a (100) edge surface for the polarization with $E \parallel [001]$. (a) shows spectra for (i) a sample annealed in a D_2 ambient and [(ii) and (iii)] then subsequently annealed in a flowing Ar ambient at the temperatures shown. (b) shows spectra similar to those shown in (a) except for a sample annealed initially in an H_2 ambient.

in flowing inert gas at 200^0C. The dominant lines at 2546.5 cm^{-1} and 3437.0 cm^{-1} are grealy strengthened by the anneal at 400^0C in an inert ambient at the expense of all of the other O-H and O-D lines seen at higher frequencies.

The discovery that several additional O-H and O-D IR lines can be converted into the dominant O-H and O-D defects by an anneal at 400^0C shows that these defects can be a source of the "hidden" hydrogen in Ga_2O_3 discussed in Sec. 3.4.1 above. The lines, with their transition moments perpendicular to the $(\bar{2}01)$ face ($E \parallel [\bar{1}\,0\,2.3]$) of the Ga_2O_3 sample, would not have been seen in earlier experiments with $\mathbf{k} \perp (\bar{2}01)$.

Data shown in Fig. 3.20 are the free-carrier absorption spectra that correspond

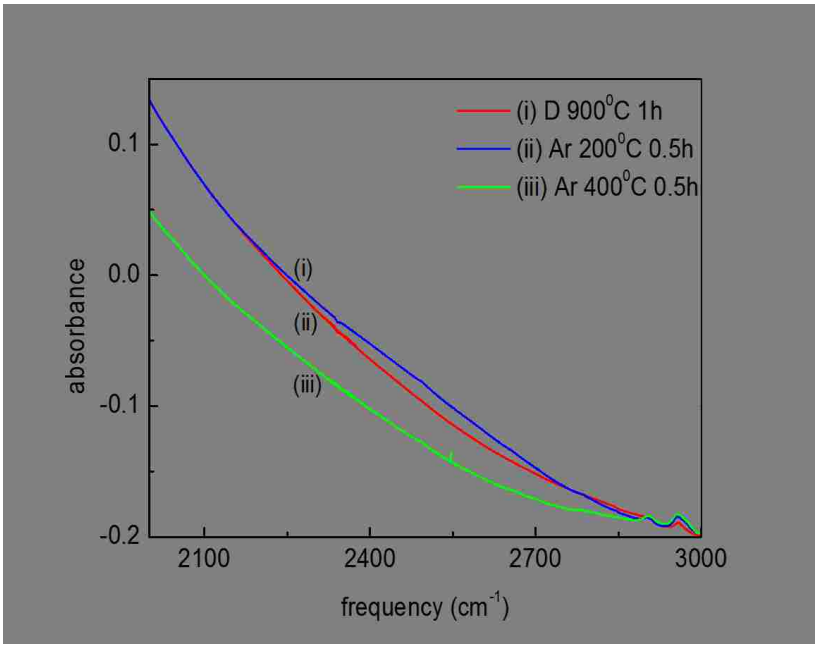

Figure 3.20: Polarized IR absorption spectra (77 K, resolution 0.5 cm^{-1}) for Ga_2O_3 samples from the Tamura Corp. that had been annealed at 900^0C in a D_2 ambient. This sample was subsequently annealed in Ar at the temperatures indicated. It shows the absorption due to free carriers that corresponds to the O-D vibrational lines in Fig. 3.19 (a).

to the O-D vibrational lines in Fig. 3.19 (a). Spectrum (i) in Fig. 3.20 shows the free-carrier absorption for a Ga_2O_3 sample that had been annealed at 900^0C in a D_2 ambient. Spectrum (ii) shows that the free-carrier absorption stays constant after a subsequent anneal at 200^0C in an inert ambient. Spectrum (iii) shows that the free-carrier absorption is reduced by an additional anneal at 400^0C in an inert ambient.

These results agree with previous findings in Section 3.4.3 that an H-related shallow donor introduced by the anneal in H_2 or D_2 is converted into the 3437 cm^{-1} O-H or 2546.5 cm^{-1} O-D center by a subsequent anneal at 400^0C in an inert ambient.

While the new O-H centers we have discovered and an H-related shallow donor (H_i or H_O) can be sources of hidden hydrogen in Ga_2O_3, they do not rule out other

possibilities such as the H_2 defect that also would not give rise to O-H absorptions lines but that could be transformed into O-H centers upon annealing.

3.5.2 Number of hydrogen atoms

Ga_2O_3 samples that contain both H and D provide additional information about the number of H (or D) atoms that a defect contains. We have examined the additional O-D centers shown in Fig. 3.17 (a) for samples annealed in ambients that contained both H_2 and D_2.

In fig. 3.21 upper panel (a), spectra were measured in the $E \parallel [001]$ polarization for the sample annealed in a D_2 (blue) or an $H_2 + D_2$ (red) ambient for $1\,h$ at 900^0C. It shows the dominant O-D vibrational lines (at 2546.5 and 2547.2 cm^{-1}) that had been seen and deemed to be the signature of a defect that contains two identical D atoms (as explained in Section 3.2.1). Fig. 3.21 (b) shows shifts of the 2603.1 and 2620.1 cm^{-1} vibrational lines after being strengthened by a subsequent anneal for $0.5\,h$ at 200^0C in flowing air indicating that these two lines are due to defects more complicated than an O-D center with a single D atom. Fig. 3.22 spectrum (i) and (ii) show the polarized spectra in the O-H stretching region of the same sample annealed in an $H_2 + D_2$ ambient for $1\,h$ at 900^0C. Spectrum (iii) shows the splitting of the 3437.0 and 3438.2 cm^{-1} pair as well. The signal to noise ratio for the OH spectra shown in Fig. 3.22 is not large enough to uncover any additional line splittings.

To better control the cooling rate of the sealed ampoule after the treatment in the $H_2 + D_2$ ambient at 900^0C, we buried the ampoule in loose sand at room temperature on top of a metal plate after taking it out of the furnace. Fig. 3.23 (a) spectrum (i) shows additional features (2610.5 and 2611.7 cm^{-1}) after the 900^0C anneal in an $H_2 + D_2$ ambient was done for a Ga_2O_3 sample that had been repeatedly annealed in H_2 or D_2 ambients. Spectrum (ii) in Fig. 3.23 (a) shows that the weaker lines were not strengthened by a subsequent anneal in flowing Ar gas at 200^0C, and spectrum (iii) shows that the dominant 2546.5 cm^{-1} line was increased in intensity after the 400^0C anneal at the expense of all of the other lines seen at

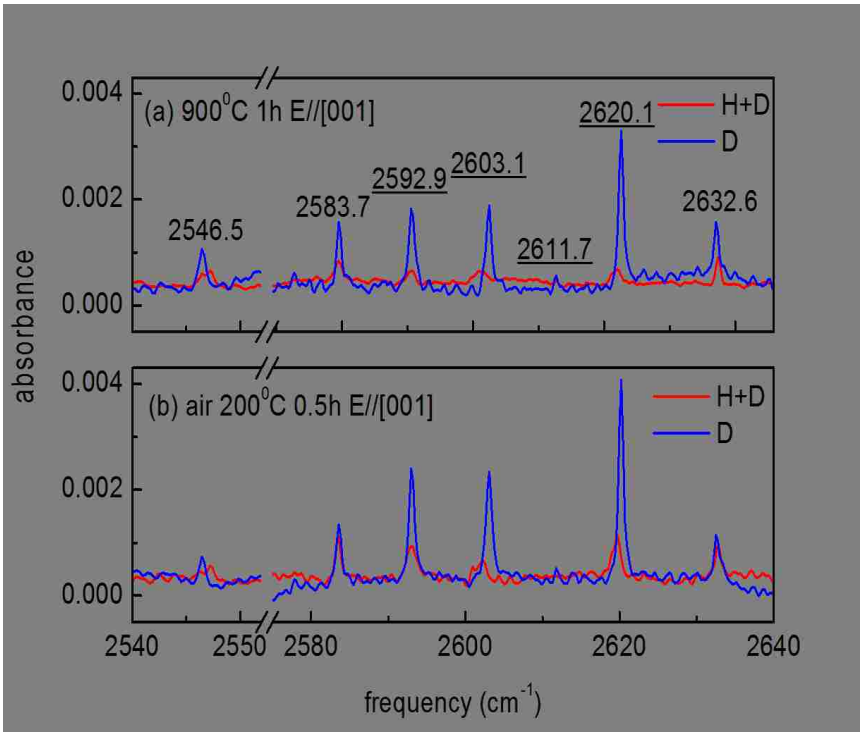

Figure 3.21: Polarized IR absorption spectra ($T = 77\,K$, resolution $= 0.5\,cm^{-1}$) for a Ga_2O_3 sample from the Tamura Corp. that had been annealed in a D_2 ambient. (a) Spectra were measured for the sample annealed in a D_2 (blue) or H_2 + D_2 (red) ambient for $1\,h$ at 900^0C; (b) spectra for the same sample after a subsequent anneal for $0.5\,h$ at 200^0C in flowing air.

higher frequencies. Fig. 3.23 (b) shows the corresponding O-H region of this sample. The OH spectra have a lower signal-to-noise ratio than the O-D spectra but show the same general behavior.

Fig. 3.23 (c) is the free-carrier absorption that corresponds to the O-D and O-H vibrational lines in Fig. 3.23 (a) and (b). It shows similar results as Fig. 3.20 supporting the conclusion that an H-related shallow donor introduced by the anneal in H_2 or D_2 is converted into the $3437\,cm^{-1}$ O-H or $2546.5\,cm^{-1}$ O-D center by a subsequent anneal at 400^0C in an inert ambient.

To achieve better signal to noise ratio in the O-H stretching region and to better

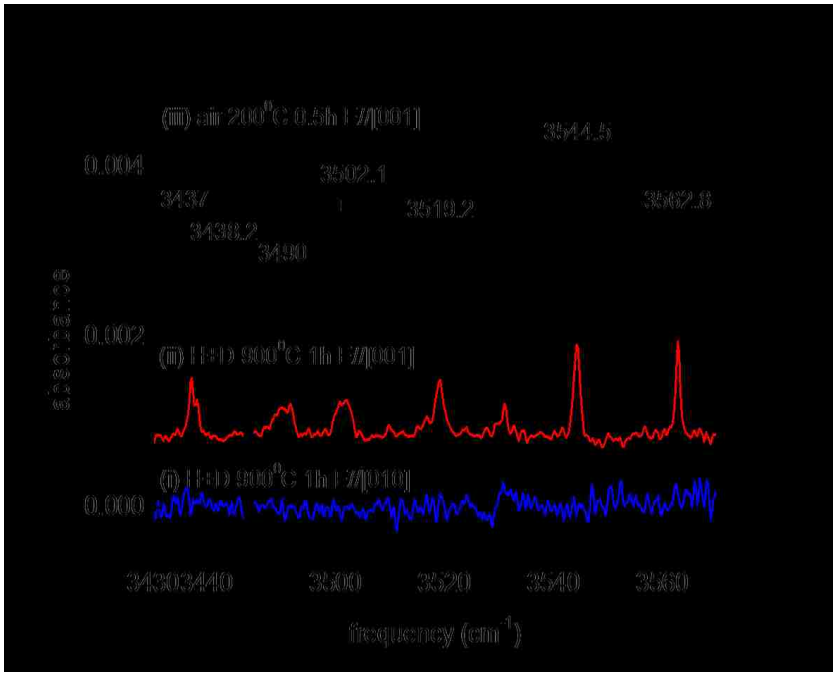

Figure 3.22: Polarized IR absorption spectra ($T = 77\,K$, resolution $= 0.5\,cm^{-1}$) for a Ga_2O_3 sample from the Tamura Corp. that had been annealed in a D_2 ambient. Spectra (i) and (ii) were measured for the sample annealed in an $H_2 + D_2$ ambient for $1\,h$ at 900^0C; spectrum (iii) for the same sample after a subsequent anneal for $0.5\,h$ at 200^0C in flowing air.

resolve the splittings, we increased the amount of H_2 in the $H_2 + D_2$ mixture and followed the 900^0C treatment by a rapid cool down of the ampoule in sand at room temperature. Figs. 3.24 (a) and (b) show that the additional lines seen for $E \parallel [001]$ were strengthened by a subsequent anneal in flowing Ar at 200^0C and that the dominant lines were increased in intensity after the 400^0C anneal at the expense of all of the other lines seen at higher frequencies. Fig. 3.24 (c) shows the corresponding free-carrier absorption, and it is consistent with all previous experiments.

Fig. 3.25 combines spectra for a sample that contained only D [spectrum (i), same as Fig. 3.17 (a) spectrum (iii)] and also for samples that contained both H and D [same as Figs. 3.23 (a) and 3.24 (a) spectra (i)]. (The spectra for O-D have

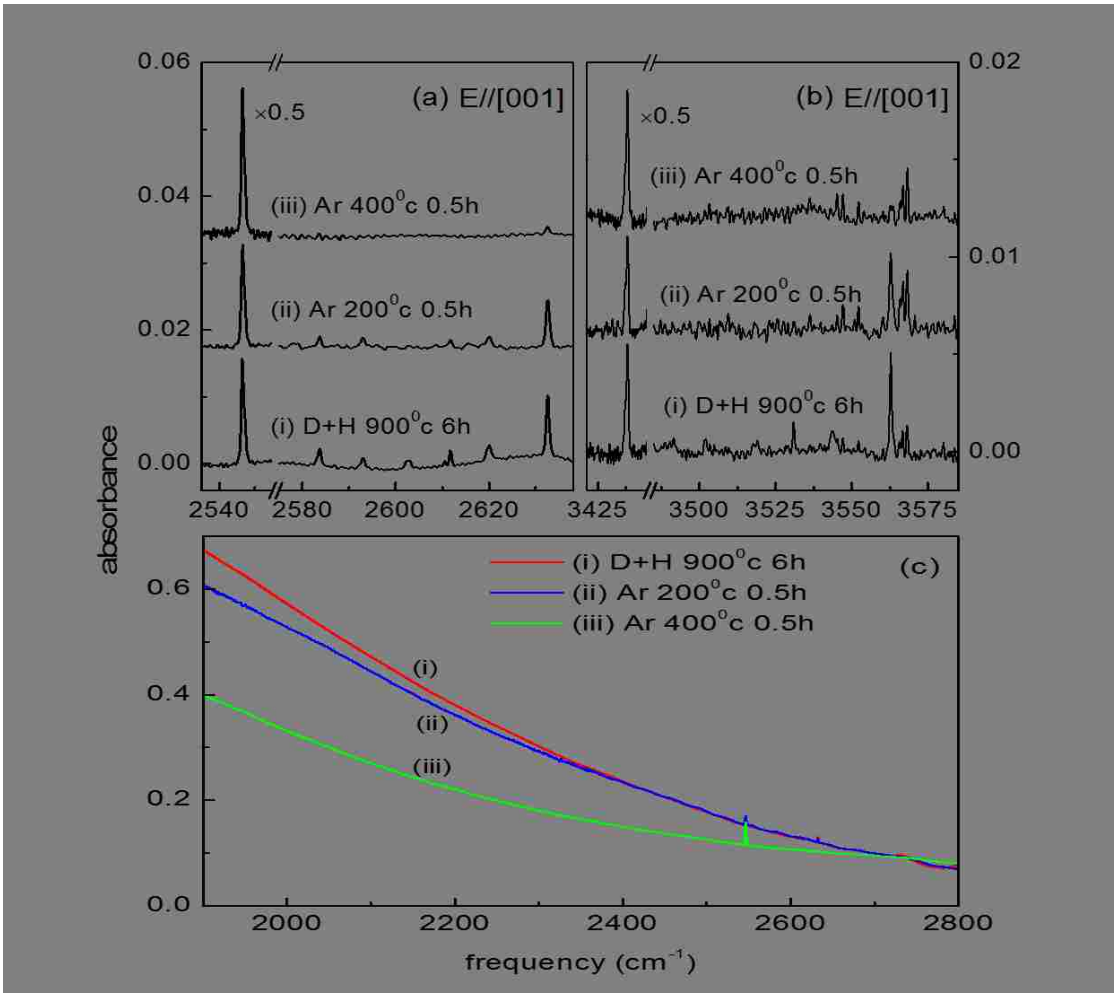

Figure 3.23: Polarized IR absorption spectra ($T = 77\,K$, resolution $= 0.5\ cm^{-1}$) for a Ga_2O_3 sample from the Tamura Corp. that had been repeatedly annealed in H_2 or D_2 ambients. Spectra (i) was measured for the sample annealed in an H_2 + D_2 ambient for $6\,h$ at 900^0C; spectrum (ii) and (iii) for the same sample after a subsequent anneal for $0.5h$ at 200^0C and 400^0C, respectively, in flowing argon. Panel (c) shows the absorption due to free carriers that corresponds to the O-H and O-D vibrational lines in Panel (a) and (b).

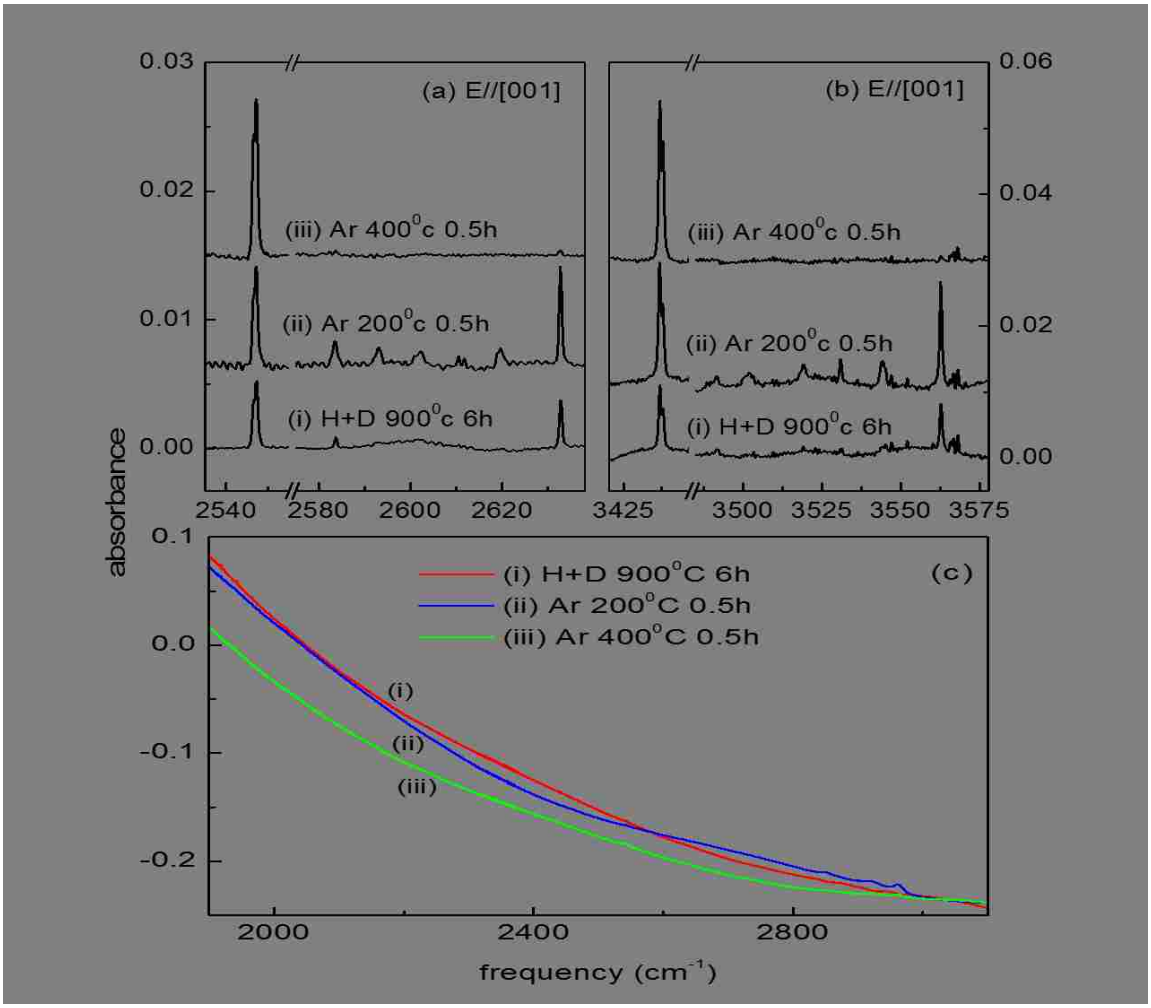

Figure 3.24: Polarized IR absorption spectra ($T = 77\,K$, resolution $= 0.5\ cm^{-1}$) for a Ga_2O_3 sample from the Tamura Corp. that had been repeatedly annealed in H_2 or D_2 ambients. Spectra (i) was measured for the sample annealed in an H_2 + D_2 ambient for $6\,h$ at 900^0C; spectrum (ii) and (iii) for the same sample after a subsequent anneal for $0.5h$ at 200^0C and 400^0C, respectively, in flowing argon. Panel (c) shows the absorption due to free carriers that corresponds to the O-H and O-D vibrational lines in Panel (a) and (b).

higher signal to noise ratio than for O-H so we focus on the O-D centers here.) The relative intensities of the lines due to V_{Ga}-2H (at 2546.4 cm^{-1}) and V_{Ga}-HD (at 2547.1 cm^{-1}) show that for spectrum (ii) the sample contained [D] $\approx$ [H] and that for spectrum (iii) the sample contained [D]>[H]. The lines labeled with red stars remain unsplit in samples that contain both H and D indicating that these defects contain a single D atom. The line at 2632.6 cm^{-1} remains especially sharp.

The O-D line at 2611.7 cm^{-1} becomes split into two lines labeled with two blue stars. The line that emerges for the sample that contains both H and D appears at 2610.5 cm^{-1}. This behavior is characteristic of a defect that contains two identical D atoms that are weakly coupled.

The lines at 2603.1 and 2620.1 cm^{-1} labeled by green stars are shifted to lower frequency in sample that contain both H and D but a clear splitting into individual components is not resolved. These line shifts are not consistent with a defect that contains a single D atom or with a defect that contains two weakly coupled D atoms. Our results that show shifted bands with unresolved splittings suggest more complicated defect structures by do not provide definitive information about the number of D atoms in these defects.

Table 3.2 summarizes the O-H and O-D vibrational frequencies we observed in Ga_2O_3 samples from Tamura Corp. that had been repeatedly annealed in H_2 or D_2 ambients. The splittings of several O-H and O-D modes suggest these defects contain two or more H(or D) atoms. The different polarization properties among them provide more information about the defect structures.

3.5.3 Candidates for additional O-H lines

Single H structures could be H_i shallow donors (see Fig. 3.26) or V_{Ga}-H structures that contain a single H atom (see Fig. 3.27). An H_i structure could explain the shallow donor seen in free-carrier-absorption spectra. H_i (D_i) could give rise to the 3562.9 (2632.6) cm^{-1} line. H_O could also be a shallow donor in these samples, but H_O is not necessary to explain our data which can be adequately explained by a H_i center(s).

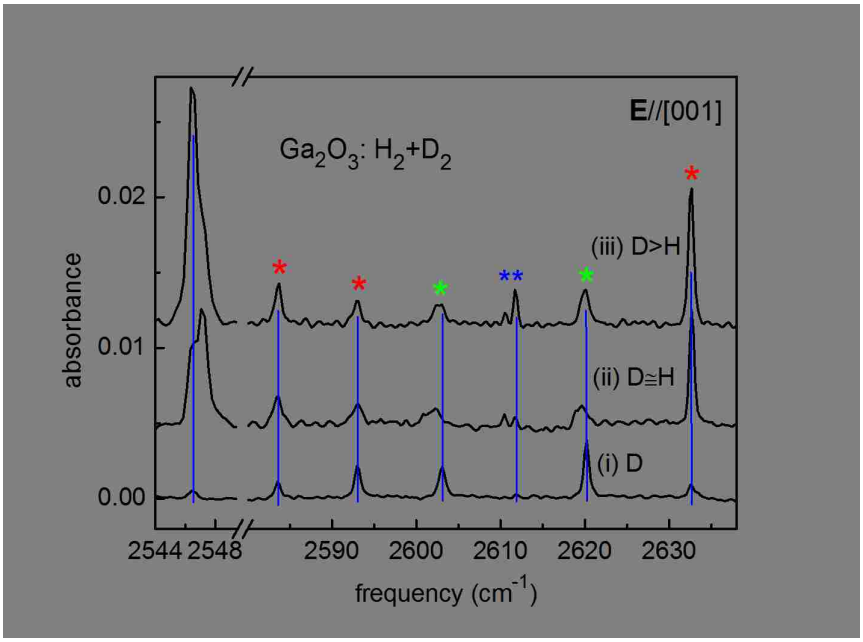

Figure 3.25: IR absorption spectra (77 K, resolution 0.5 cm^{-1}) for Ga_2O_3 samples mounted on a (100) edge surface for the polarization with $E \parallel [001]$. Samples had been annealed (i) in a D_2 ambient or [(ii) and (iii)] in an ambient containing a mixture of H_2 and D_2.

The new two H (or two D) structure 3531.1 (2611.7) cm^{-1} line could be one of the V_{Ga}-2H structures (Fig. 3.27) with transition moment normal to $(\bar{2}01)$.

H_2 remains a candidate for a hidden H species, but like H_O, H_2 is not necessary to explain our data.

Table 3.2: Frequencies of O-H and O-D IR lines seen in Ga_2O_3 containing H, D, both H and D. The ratio of the frequencies of corresponding O-H and O-D centers, $r = \omega_H/\omega_D$, is also shown.

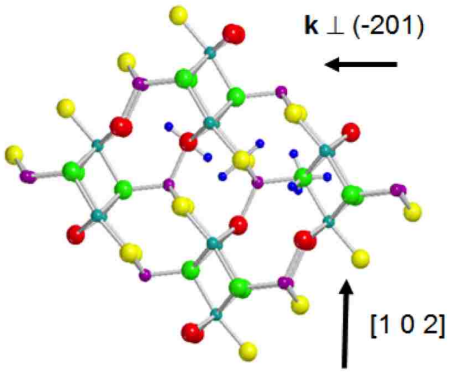

Figure 3.26: Possible hydrogen interstitial sites (in blue) in an unrelaxed Ga_2O_3 lattice

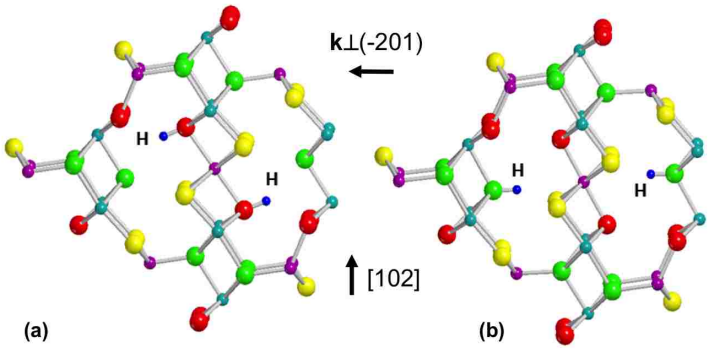

Figure 3.27: (a) and (b) show two relaxed configurations of $Ga(1)_{21}$, each with two equivalent H sites with no (010) O-H projection and with transition moments perpendicular to the $(\bar{2}01)$ plane.

3.6 Conclusion

Annealing Ga_2O_3 wafers with a $(\bar{2}01)$ face in an H_2 ambient at temperatures greater than 800^0C produces a strongly polarized O-H absorption line at $3437.0\,cm^{-1}$. Samples that contain both H and D show an additional dynamically decoupled O-H mode that is characteristic of a defect that contains two H atoms. Theory assigns the $3437.0\,cm^{-1}$ line to a particular V_{Ga}-2H complex. Corresponding results have been obtained for Ga_2O_3 samples annealed in a D_2 ambient.

Annealing Ga_2O_3 in an H_2 ambient at elevated temperature ($\backsim 900^0C$) can also produce a reservoir of hydrogen that is not seen by IR absorption measurements made with $\mathbf{k} \perp (\bar{2}01)$. This hidden reservoir of hydrogen also gives rise to free-carrier absorption that is characteristic of n-type conductivity. The further annealing of this hydrogenated sample at a lower temperature (400^0C) in an inert ambient converts this reservoir of hydrogen and its associated free-carrier absorption into the V_{Ga}-2H center that gives rise to the $3437.0\,cm^{-1}$ line.

Additional IR absorption experiments with a light beam directed with $\mathbf{k} \perp (100)$ reveal new O-H centers, several of which have transition moments that are perpendicular to the $(\bar{2}01)$ plane that would not have been seen in our earlier experiments.

These additional O-H lines have a thermal stability that is consistent with the reservoir of hidden hydrogen in Ga_2O_3 that can be converted into the 3437.0 cm^{-1} center by thermal annealing.

Experiments have been performed for Ga_2O_3 samples that contained both H and D that provide information about the number of H atoms in a defect. O-H centers that contain a single hydrogen (the 3562.9 cm^{-1} center, for example) could be H_i centers that act as shallow donors. These H_i centers could explain the free-carrier absorption that is produced by an anneal in H_2 at 900^0C and that is transformed into the 3437.0 cm^{-1} center by annealing in an inert ambient at 400^0C. O-H centers that contain a single H and with polarization normal to $(\bar{2}01)$ could also be due to V_{Ga} complexes with one of the structures shown in Fig. 3.27 with just one of the H sites occupied.

Candidates for centers that contain two identical H atoms and that have transition moments normal to the $(\bar{2}01)$ plane are the V_{Ga}-2H centers shown in Fig. 3.27.

Finally, H_O centers could act as shallow donors that can be converted into the dominant V_{Ga}-2H center (at 3437.0 cm^{-1}) by thermal annealing that would not give O-H modes in our samples. Our results also do not rule out the existence of interstitial H_2 centers not seen by IR spectroscopy that could be converted into other defects by thermal annealing. However, while our results do not rule out these possibilities, these defects are not necessary to explain our data. Further experiments will be required to investigate these additional possibilities for hydrogen centers in Ga_2O_3.

Similar to the behavior of hydrogen in the other transparent conducting oxides that have been studied in recent years, hydrogen in Ga_2O_3 reveals new defect physics. In the case of Ga_2O_3, defects that involve relaxed V_{Ga} centers play an especially prominent role in the reactions of hydrogen-containing defects that occur and in the O-H defect structures that form.

Chapter 4

Conclusion

In this chapter, we summarize the work that has been done in this dissertation on hydrogen centers in In_2O_3 and β-Ga_2O_3 bulk samples by FTIR spectroscopy.

In_2O_3 is a transparent conducting oxide that finds broad application in flat-panel displays and as transparent electrodes for electronic devices such as light emitting diodes and solar cells. Hydrogen has been found to be an n-type dopant in In_2O_3 that gives rise to unintentional conductivity.

We have performed two types of experiments to determine the diffusivity of H_i^+ in In_2O_3 from its IR absorption spectra. In_2O_3 samples were hydrogenated by annealing in an H_2 ambient at temperatures near 700 K. We have found that we can determine the diffusion depth of H_i^+ by mechanically thinning the sample and monitoring the amount of H that remains as a function of depth by measurements of the IR line at 3306 cm^{-1}. A fit of the complementary error function to the H_i^+ indiffusion profile yields the diffusivities at 723 K and 698 K.

The other type of experiment concerns the out-diffusion of the H_i^+ center. Once a thin hydrogenated layer in In_2O_3 has been produced by an anneal in an H_2 ambient, its subsequent elimination by thermal annealing in an inert ambient at various temperatures lets us determine the diffusivities (at $573 - 673\ K$) by fitting the intensity of the 3306 cm^{-1} line with the numerical solution of Fick's Second Law.

Combining the diffusivities of H_i^+ determined near 700 K by mass transport measurements (in and out-diffusion) with the data for the diffusivity of H_i^+ measured

near 160 K by measurements of the H_i^+ jump rate, our experiments probe the diffusivity of H in In_2O_3 for over 11 decades.

β-Ga_2O_3 shows unintentional n-type conductivity and is attracting much recent attention as a promising transparent conducting oxide with an ultra-wide band-gap (UWBG). Theory predicts that O vacancies are not shallow donors and suggests that hydrogen impurities can be a cause of n-type behavior. Both interstitial H and H trapped at an oxygen vacancy are predicted to be shallow donors. We have recently discovered an O-H vibrational line at 3437 cm^{-1} in β-Ga_2O_3. This line was found to be strongly polarized along the [102] direction of a $(\bar{2}01)$-oriented wafer and has been assigned to a V_{Ga}-2H complex. Surprisingly, this defect has been found to be most effectively produced by a two-step annealing process. A first anneal in an H_2 ambient at 900^0C produces a weak line at 3437 cm^{-1}. A second anneal in flowing N_2 at 400^0C greatly increases the intensity of the 3437 cm^{-1} line. These results show that a hidden form of H can be produced in Ga_2O_3 that can be converted into the V_{Ga}-2H complex by an additional thermal annealing treatment in an inert ambient. Similarly, the implantation of protons into Ga_2O_3 at room temperature produces a weak line at 3437 cm^{-1} that is made roughly 4 times more intense by a subsequent anneal at 400^0C.

Additional IR vibrational modes were discovered both in the polarization direction along [102] and [001] directions in Ga_2O_3 samples that had been repeatedly treated in H_2 or D_2 ambients by rotating the $(\bar{2}01)$-oriented wafer around its [010] axis and by controlling the cooling rate after the anneal at 900^0C in H_2 or D_2 ambients. These additional IR lines disappeared after the 400^0C anneal in an inert ambient while the dominant line at 3437 cm^{-1} or 2546.5 cm^{-1} increased in intensity. Meanwhile, this 400^0C anneal in an inert ambient reduces the free-carrier absorption in these samples.

These results suggest that an H-related shallow donor introduced by the anneal in H_2 is converted into the 3437 cm^{-1} O-H center by a subsequent anneal at 400^0C in an inert ambient. Interstitial hydrogen (H_i) or hydrogen trapped at oxygen vacancy (H_o) predicted by theory are good candidates for such H-related shallow donors that might serve as a reservoir of hidden hydrogen that can be produced by annealing

a Ga_2O_3 sample in an H_2 ambient. However, these results do not eliminate other possibilities (like H_2 molecules) that may also provide a reservoir of hydrogen in our samples that are difficult to observe directly.

While we have made excellent progress revealing new hydrogen centers in Ga_2O_3 and determining their effect on conductivity, additional experiments and complementary theory will be required to identify the H-related defects in Ga_2O_3, the role they play, and their complicated reaction chemistry.

Appendix

In this Appendix, a Mathematica program for simulating hydrogen diffusion process is shown.

```
(*fitting 400c out-diffusion data (sample#30)
  by minimizing the sum of squares of the
  deviations between the measured data and
  the results of this diffusion model*)
(*Df is the diffusion constant (cm^2/h);
x2 is sample thickness (cm);
t2 is diffusion time; data4003 is the measured
 data (outdiffusing time and its corresponding
   integrated absorbance) (normalized);
data4004 is the calculated integrated
 absorbance (normalized);
SUMXMY2 is the sum of squares of the
 deviations between data4003 and data4004*)
Df = 1.112 * 10 ^ (-6); x2 = 0.05; t2 = 36;
f = 5;
s1 = NDSolve[
    {D[y[t, x], t] == Df D[y[t, x], x, x], y[0, x] ==
      3.34302 ((Erfc[x / 0.0038630412569999883] -
            Exp[-100 000 x]) * (1 - Exp[-1000 (x2 - x)]) +
         (Erfc[(x2 - x) / 0.0038630412569999883] - Exp[
             -100 000 (x2 - x)]) * (1 - Exp[-1000 (x)])),
     y[t, 0] == 0, y[t, x2] == 0}, y, {t, 0, t2},
    {x, 0, x2}, Method → {"MethodOfLines",
      "SpatialDiscretization" →
       {"TensorProductGrid", "MinPoints" → 200}}];
```

```
Plot[{Evaluate[y[t2 / f / f / f / f / f, x] /. s1],
  Evaluate[y[t2 / f / f / f / f, x] /. s1],
  Evaluate[y[t2 / f / f / f, x] /. s1],
  Evaluate[y[t2 / f / f, x] /. s1],
  Evaluate[y[t2 / f, x] /. s1]},
 {x, 0, 0.015}, PlotRange → {0, 3.3},
 PlotStyle → {Black}, AspectRatio → 5 / 4,
 Axes → True, AxesStyle → {Black, Bold},
 Frame → True, FrameStyle → Thick,
 FrameTicks → {{{0, 1, 2, 3}, None},
   {{0, 0.005, 0.010, 0.015}, None}},
 LabelStyle → {24, GrayLevel[0]}]
```

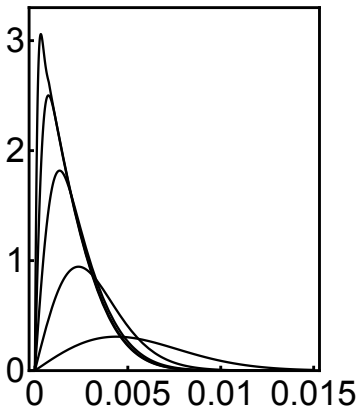

```
s1 = NDSolve[{D[y[t, x], t] == Df D[y[t, x], x, x],
    y[0, x] == 272.7674950094528
      ((Erfc[x / 0.0038630412569999883] -
           Exp[-100 000 x]) * (1 - Exp[-1000 (x2 - x)]) +
        (Erfc[(x2 - x) / 0.0038630412569999883] - Exp[
            -100 000 (x2 - x)]) * (1 - Exp[-1000 (x)])),
    y[t, 0] == 0, y[t, x2] == 0}, y, {t, 0, t2},
   {x, 0, x2}, Method → {"MethodOfLines",
     "SpatialDiscretization" →
      {"TensorProductGrid", "MinPoints" → 200}}];
data4003 = {{0, 1}, {0.25, 0.809697915},
   {0.5, 0.723727356}, {1, 0.646647227},
   {2, 0.467862744}, {4, 0.42251084},
   {8, 0.323907231}, {12, 0.229748172},
   {24, 0.150810664}, {36, 0.155564008}};
data4004 = Table[{t, (1 / 1.1455144551136704`) *
     Integrate[Evaluate[y[t, x] /. s1],
       {x, 0, x2}][[1]]}, {t, 0, t2, 0.25}];
SUMXMY2 = Total[(data4003[[2 ;; 10, 2]] -
     {data4004[[2, 2]], data4004[[3, 2]],
      data4004[[5, 2]], data4004[[9, 2]],
      data4004[[17, 2]], data4004[[33, 2]],
      data4004[[49, 2]], data4004[[97, 2]],
      data4004[[145, 2]]}) ^ 2]
df =
 Df /
  3600
```

```
0.00594132
```

$$3.08889 \times 10^{-10}$$

```
Show[ListLinePlot[data4004, PlotRange → {0.05, 1.1},
  PlotStyle → {Black, Thick}],
 ListPlot[data4003, PlotRange → All,
  PlotStyle → {Black, PointSize[0.04]}],
 Axes → True, AxesStyle → {Black, Bold},
 Frame → True, FrameStyle → Thick,
 FrameTicks → {{None, {0.2, 0.4, 0.6, 0.8, 1.0}},
   {{0, 10, 20, 30, 40}, None}},
 LabelStyle → {24, GrayLevel[0]}, AspectRatio → 5 / 4]
```

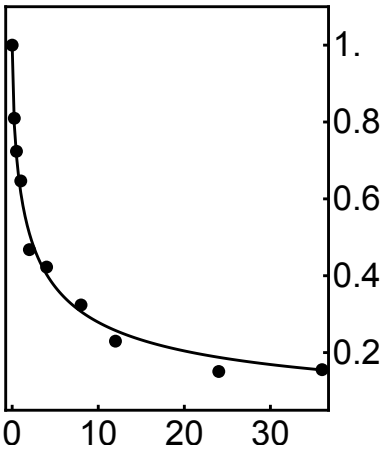

Bibliography

[1] P Weiser, Y Qin, W Yin, M Stavola, WB Fowler, and LA Boatner. Symmetry and diffusivity of the interstitial hydrogen shallow-donor center in In_2O_3. *Applied Physics Letters*, 109(20):202105, 2016.

[2] BG Lewis and DC Paine. Applications and processing of transparent conducting oxides. *MRS bulletin*, 25(8):22–27, 2000.

[3] M Stavola. Local vibrational mode spectroscopy of impurities in semiconductors. *in Encyclopedia of Materials: Science and Technology, edited by K.H.J. Buschow, R.W. Cahn, M.C. Flemings, B. Ilschner, E.J. Kramer, and S. Mahajan (Elsevier, Amsterdam)*, 2001.

[4] AS Barker Jr and AJ Sievers. Optical studies of the vibrational properties of disordered solids. *Reviews of Modern Physics*, 47(S2):S1, 1975.

[5] RC Newman. *Infra-red studies of crystal defects*. Taylor & Francis; Barnes & Noble Books, 1973.

[6] HY Fan. Infra-red absorption in semiconductors. *Reports on Progress in Physics*, 19(1):107, 1956.

[7] M Fox. Optical properties of solids. Oxford master series in condensed matter physics, 2001.

[8] R Murray and RC Newman. in Landolt-Bornstein, new series, edited by O. Madelung and M. Schulz. *Springer-Verlag, Berlin*, 22b, 1989.

[9] PR Griffiths and JA de Haseth. Fourier transform infrared spectrometry. *Wiley-Interscience, New York*, 1986.

[10] Bomem inc. Bomem spectrometer system and software users manual. 1993.

[11] M Stavola and WB Fowler. Tutorial: Novel properties of defects in semiconductors revealed by their vibrational spectra. *Journal of Applied Physics*, 123 (16):161561, 2018.

[12] PG Dawber and RJ Elliott. Theory of optical absorption by vibrations of defects in silicon. *Proceedings of the Physical Society*, 81(3):453, 1963.

[13] DM Kozuch, M Stavola, SJ Pearton, CR Abernathy, and WS Hobson. Passivation of carbon-doped gaas layers by hydrogen introduced by annealing and growth ambients. *Journal of applied physics*, 73(8):3716–3724, 1993.

[14] RC Newman and ER Weber. *in Imperfections in III-V Materials*, volume 38. edited by E. Weber, Academic Press, Boston, 1993.

[15] PY Yu and M Cardona. *Fundamentals of semiconductors: physics and materials properties*. Springer Science & Business Media, 2010.

[16] HY Fan. Effects of free carriers on the optical properties, chapt. 9 in, optical properties of III-V compounds, edited by R.K. Willardson and A.C. Beer. In *Semiconductors and Semimetals*, volume 3, pages 405–419. Academic, New York, 1967.

[17] SJ Pearton, JW Corbett, and M Stavola. *Hydrogen in crystalline semiconductors*, volume 16. Springer Science & Business Media, 2013.

[18] CG Van de Walle. Hydrogen as a cause of doping in zinc oxide. *Physical review letters*, 85(5):1012, 2000.

[19] C Kılıc and A Zunger. N-type doping of oxides by hydrogen. *Applied physics letters*, 81(1):73–75, 2002.

[20] A Janotti and CG Van de Walle. Hydrogen multicentre bonds. *Nature materials*, 6(1):44, 2007.

[21] AK Singh, A Janotti, M Scheffler, and CG Van de Walle. Sources of electrical conductivity in SnO_2. *Physical Review Letters*, 101(5):055502, 2008.

[22] S Limpijumnong, P Reunchan, A Janotti, and CG Van de Walle. Hydrogen doping in indium oxide: An ab initio study. *Physical Review B*, 80(19):193202, 2009.

[23] JB Varley, JR Weber, A Janotti, and CG Van de Walle. Oxygen vacancies and donor impurities in β-Ga_2O_3. *Applied Physics Letters*, 97(14):142106, 2010.

[24] JB Varley, H Peelaers, A Janotti, and CG Van de Walle. Hydrogenated cation vacancies in semiconducting oxides. *Journal of Physics: Condensed Matter*, 23 (33):334212, 2011.

[25] GA Shi, M Saboktakin, M Stavola, and SJ Pearton. Hidden hydrogen in as-grown ZnO. *Applied physics letters*, 85(23):5601–5603, 2004.

[26] EV Lavrov, F Herklotz, and J Weber. Identification of hydrogen molecules in ZnO. *Physical review letters*, 102(18):185502, 2009.

[27] CG Van de Walle. Defect analysis and engineering in ZnO. *Physica B: Condensed Matter*, 308:899–903, 2001.

[28] EV Lavrov, J Weber, F Börrnert, CG Van de Walle, and R Helbig. Hydrogen-related defects in ZnO studied by infrared absorption spectroscopy. *Physical Review B*, 66(16):165205, 2002.

[29] GA Shi, M Stavola, SJ Pearton, M Thieme, EV Lavrov, and J Weber. Hydrogen local modes and shallow donors in ZnO. *Physical Review B*, 72(19):195211, 2005.

[30] EV Lavrov, F Herklotz, and J Weber. Identification of two hydrogen donors in ZnO. *Physical Review B*, 79(16):165210, 2009.

[31] SG Koch, EV Lavrov, and J Weber. Interplay between interstitial and substitutional hydrogen donors in ZnO. *Physical Review B*, 89(23):235203, 2014.

[32] SG Koch, EV Lavrov, and J Weber. Photoconductive detection of tetrahedrally coordinated hydrogen in ZnO. *Physical Review Letters*, 108(16):165501, 2012.

[33] F Herklotz, A Hupfer, KM Johansen, BG Svensson, SG Koch, and EV Lavrov. Infrared absorption on a complex comprising three equivalent hydrogen atoms in ZnO. *Physical Review B*, 92(15):155203, 2015.

[34] I Hamberg and CG Granqvist. Evaporated Sn-doped In_2O_3 films: Basic optical properties and applications to energy-efficient windows. *Journal of Applied Physics*, 60(11):R123–R160, 1986.

[35] BG Svensson, SJ Pearton, and C Jagadish. Oxide semiconductors, 2013.

[36] PDC King, RL Lichti, YG Celebi, JM Gil, RC Vilão, HV Alberto, JP Duarte, DJ Payne, RG Egdell, I McKenzie, et al. Shallow donor state of hydrogen in In_2O_3 and SnO_2: Implications for conductivity in transparent conducting oxides. *Physical Review B*, 80(8):081201, 2009.

[37] T Koida, H Fujiwara, and M Kondo. Hydrogen-doped In_2O_3 as high-mobility transparent conductive oxide. *Japanese Journal of Applied Physics*, 46(7L): L685, 2007.

[38] T Koida, H Sai, and M Kondo. Application of hydrogen-doped In_2O_3 transparent conductive oxide to thin-film microcrystalline Si solar cells. *Thin Solid Films*, 518(11):2930–2933, 2010.

[39] B Macco, MA Verheijen, LE Black, B Barcones, J Melskens, and WMM Kessels. On the solid phase crystallization of In_2O_3: H transparent conductive oxide films prepared by atomic layer deposition. *Journal of Applied Physics*, 120(8): 085314, 2016.

[40] W Yin, K Smithe, P Weiser, M Stavola, WB Fowler, L Boatner, SJ Pearton, DC Hays, and SG Koch. Hydrogen centers and the conductivity of In_2O_3 single crystals. *Physical Review B*, 91(7):075208, 2015.

[41] M Stavola. *Identification of Defects in Semiconductors, edited by M. Stavola*. Academic Press, San Diego, 1999.

[42] AA Kaplyanskii. Noncubic centers in cubic crystals and their piezospectroscopic investigation. *Optics and Spectroscopy*, 16:329, 1964.

[43] G Davies, EC Lightowlers, M Stavola, K Bergman, and B Svensson. The $3942cm^{-1}$ optical band in irradiated silicon. *Physical Review B*, 35(6):2755, 1987.

[44] M Stavola, SJ Pearton, J Lopata, CR Abernathy, and K Bergman. Stress experiments that combined stress splittings to determine defect symmetry and stress alignment to probe defect motion were performed for the Be-H complex in GaAs. *Phys. Rev. B*, 39:8051, 1989.

[45] JW Corbett, RS McDonald, and GD Watkins. The configuration and diffusion of isolated oxygen in silicon and germanium. *Journal of Physics and Chemistry of Solids*, 25(8):873–879, 1964.

[46] B Tuck. Introduction to diffusion in semiconductors. Peter Peregrinus, Stevenage, 1974.

[47] RJ Borg and GJ Dienes. An introduction to solid state diffusion. *Academic Press, San Diego*, 1988.

[48] JD Plummer, MD Deal, and PB Griffin. Silicon VLSI technology: fundamentals, practice, and modeling. *Prentice Hall Inc, Upper Saddle River*, 2000.

[49] JP Remeika and EG Spencer. Electrical conductivity and growth of single-crystal indium sesquioxide. *Journal of Applied Physics*, 35(10):2803–2803, 1964.

[50] DR Hagleitner, M Menhart, P Jacobson, S Blomberg, K Schulte, E Lundgren, M Kubicek, J Fleig, F Kubel, C Puls, et al. Bulk and surface characterization of In_2O_3 (001) single crystals. *Physical Review B*, 85(11):115441, 2012.

[51] Air Products. Operating manual for air products liquid transfer LT-3 helitran cryostat.

[52] R Dovesi, VR Saunders, C Roetti, R Orlando, CM Zicovich-Wilson, F Pascale, B Civalleri, K Doll, NM Harrison, IJ Bush, et al. CRYSTAL06 users manual (Università di Torino, Torino, 2006). *Google Scholar*, 1999.

[53] Y Qin, P Weiser, K Villalta, M Stavola, WB Fowler, I Biaggio, and L Boatner. Diffusivity of the interstitial hydrogen shallow donor in In_2O_3. *Journal of Applied Physics*, 123(16):161506, 2018.

[54] MA Mastro, A Kuramata, J Calkins, J Kim, F Ren, and SJ Pearton. Perspectiveopportunities and future directions for Ga_2O_3. *ECS Journal of Solid State Science and Technology*, 6(5):P356–P359, 2017.

[55] M Higashiwaki, A Kuramata, H Murakami, and Y Kumagai. State-of-the-art technologies of gallium oxide power devices. *Journal of Physics D: Applied Physics*, 50(33):333002, 2017.

[56] M Higashiwaki and GH Jessen. Guest editorial: The dawn of gallium oxide microelectronics. *Applied Physics Letters*, 112:060401, 2018.

[57] JY Tsao, S Chowdhury, MA Hollis, D Jena, NM Johnson, KA Jones, RJ Kaplar, S Rajan, CG Van de Walle, E Bellotti, et al. Ultrawide-bandgap semiconductors: Research opportunities and challenges. *Advanced Electronic Materials*, 4 (1):1600501, 2018.

[58] SJ Pearton, J Yang, PH Cary IV, F Ren, J Kim, MJ Tadjer, and MA Mastro. A review of Ga_2O_3 materials, processing, and devices. *Applied Physics Reviews*, 5(1):011301, 2018.

[59] M Higashiwaki, K Sasaki, H Murakami, Y Kumagai, A Koukitu, A Kuramata, T Masui, and S Yamakoshi. Recent progress in Ga_2O_3 power devices. *Semiconductor Science and Technology*, 31(3):034001, 2016.

[60] M Stavola, WB Fowler, Y Qin, P Weiser, and SJ Pearton. *Hydrogen in Ga_2O_3, Chapt. 9 in Ga_2O_3 Growth, Processing and Devices, edited by S.J. Pearton, F. Ren, and M. Mastro.* Elsevier, to be published, 2018.

[61] M Higashiwaki, K Sasaki, A Kuramata, T Masui, and S Yamakoshi. Gallium oxide (Ga_2O_3) metal-semiconductor field-effect transistors on single-crystal β-Ga_2O_3 (010) substrates. *Applied Physics Letters*, 100(1):013504, 2012.

[62] M Higashiwaki, K Sasaki, A Kuramata, T Masui, and S Yamakoshi. Development of gallium oxide power devices. *physica status solidi (a)*, 211(1):21–26, 2014.

[63] M Orita, H Ohta, M Hirano, and H Hosono. Deep-ultraviolet transparent conductive β-Ga_2O_3 thin films. *Applied Physics Letters*, 77(25):4166–4168, 2000.

[64] S Ohira, N Suzuki, N Arai, M Tanaka, T Sugawara, K Nakajima, and T Shishido. Characterization of transparent and conducting sn-doped β-Ga_2O_3 single crystal after annealing. *Thin Solid Films*, 516(17):5763–5767, 2008.

[65] J Yang, S Ahn, F Ren, SJ Pearton, S Jang, J Kim, and A Kuramata. High reverse breakdown voltage schottky rectifiers without edge termination on Ga_2O_3. *Applied Physics Letters*, 110(19):192101, 2017.

[66] Q He, W Mu, H Dong, S Long, Z Jia, H Lv, Q Liu, M Tang, X Tao, and M Liu. Schottky barrier diode based on β-Ga_2O_3 (100) single crystal substrate and its temperature-dependent electrical characteristics. *Applied Physics Letters*, 110 (9):093503, 2017.

[67] MR Lorenz, JF Woods, and RJ Gambino. Some electrical properties of the semiconductor β-Ga_2O_3. *Journal of Physics and Chemistry of Solids*, 28(3): 403–404, 1967.

[68] PDC King, I McKenzie, and TD Veal. Observation of shallow-donor muonium in Ga_2O_3: Evidence for hydrogen-induced conductivity. *Applied Physics Letters*, 96(6):062110, 2010.

[69] YG Celebi, RL Lichti, BB Baker, PW Mengyan, HN Bani-Salameh, and E Catak. Muonium dynamics in transparent conducting oxides. *Physica B: Condensed Matter*, 407(15):2879–2882, 2012.

[70] P Weiser, M Stavola, WB Fowler, Y Qin, and S Pearton. Structure and vibrational properties of the dominant OH center in β-Ga_2O_3. *Applied Physics Letters*, 112(23):232104, 2018.

[71] F Bekisli, M Stavola, WB Fowler, L Boatner, E Spahr, and G Lüpke. Hydrogen impurities and shallow donors in SnO_2 studied by infrared spectroscopy. *Physical Review B*, 84(3):035213, 2011.

[72] F Bekisli, WB Fowler, M Stavola, LA Boatner, E Spahr, and G Lüpke. Bond angles for OH defects in SnO_2 from polarization properties of their vibrational modes. *Physical Review B*, 85(20):205202, 2012.

[73] S Geller. Crystal structure of β-Ga_2O_3. *The Journal of Chemical Physics*, 33 (3):676–684, 1960.

[74] J Åhman, G Svensson, and J Albertsson. A reinvestigation of β-gallium oxide. *Acta Crystallographica Section C: Crystal Structure Communications*, 52(6): 1336–1338, 1996.

[75] BE Kananen, LE Halliburton, KT Stevens, GK Foundos, and NC Giles. Gallium vacancies in β-Ga_2O_3 crystals. *Applied Physics Letters*, 110(20):202104, 2017.

[76] T Zacherle, PC Schmidt, and M Martin. Ab initio calculations on the defect structure of β-Ga_2O_3. *Physical Review B*, 87(23):235206, 2013.

[77] P Deák, QD Ho, F Seemann, B Aradi, M Lorke, and T Frauenheim. Choosing the correct hybrid for defect calculations: A case study on intrinsic carrier trapping in β- Ga_2O_3. *Physical Review B*, 95(7):075208, 2017.

[78] A Kyrtsos, M Matsubara, and E Bellotti. Migration mechanisms and diffusion barriers of vacancies in Ga_2O_3. *Physical Review B*, 95(24):245202, 2017.

[79] P Ugliengo. MOLDRAW: A program to display and manipulate molecular and crystal structures. *Torino, 2006 available on the web at: http: www. moldraw. unito. it*, 2006.

[80] E Korhonen, F Tuomisto, D Gogova, G Wagner, M Baldini, Z Galazka, R Schewski, and M Albrecht. Electrical compensation by Ga vacancies in Ga_2O_3 thin films. *Applied Physics Letters*, 106(24):242103, 2015.

[81] M Wöhlecke and L Kovács. OH^- ions in oxide crystals. *Critical Reviews in Solid State and Material Sciences*, 26(1):1–86, 2001.

Vita

Ying Qin was born and raised in Tianjin, China. She started her undergraduate study in Physics at Nankai University and received her Bachelor's degree in Physics in June 2012. She was enrolled in the Ph.D. program in the Physics Department at Lehigh University in August 2013 and obtained her Master of Science Engineering degree in Electrical Engineering in May 2016. She began her Ph.D. research with Dr. Michael Stavola in the summer of 2014, focusing on hydrogen defects in semiconducting oxides. She obtained her PhD in January 2019.